POLITECNICO DI TORINO



DIATI DEPARTMENT - MASTER OF SCIENCE IN GEORESOURCES AND GEOENERGY ENGINEERING

CONSTITUTIVE MODEL PREDICTIONS FOR DRILLING ANISOTROPIC SHALE: A COMPARATIVE STUDY

SUPERVISORS: CANDIDATE:

CHIARA DEANGELI DANIELE MARTINELLI Roberto Margiotta (s333087)

Academic Year: 2024/2025

Abstract

This experimental thesis delves into the study of Tournemire Shale, in particular it investigates failure mechanisms and wellbore integrity during drilling operations through a comparative approach using several constitutive models integrated in FLAC2D 8.1 (Fast Lagrangian Analysis of Continua, FDM). Shale formations are most often found as cap rocks in reservoirs, which makes their structural and hydraulic integrity vital, especially given their important role in the geological storage of CO₂, H₂ and CH₄ in the current energy transition. The methodological approach found its basis on a validation check between the analytical solution of Kirsch and the first, simple but essential Isotropic Linear Elastic model under dry conditions implemented in the software. This step was crucial to maintain a rigorous framework for the following models. Mesh and boundary conditions for radial and tangential effective stresses were verified in sectors A ($\theta = 0^{\circ}$, along $\sigma_{H,\text{max}}$) and B ($\theta = 90^{\circ}$, along $\sigma_{h,\min}$). The analysis was then extended to Transversely Isotropic Elastic (TIE), Isotropic Linear Elastic with Mohr-Coulomb (ILE-MC), Ubiquitous-Joint with weak-plane mechanics (UBI), and Transversely Isotropic Elastic with weak-plane mechanics (CANISO), incorporating dry, drained, and undrained conditions, together with variations in pore pressure p_w and rotation of far-field stresses. In summary, the numerical simulations show consistent predictions of failure mechanisms in line with typical shale trends, with shear concentrating in the rock matrix and potential slip along weakness planes. Sector B is generally the most stressed; in some cases, local tensile zones are observed along the wall in sector B, a topic critically discussed in this work and deserving further investigation. Overall, the multi-model comparison clarifies load—response trends and highlights key factors for future research.

Contents

1	Intr	roduction	8
	1.1	Overview	8
	1.2	Shale Geomechanics in a Transitioning Energy Sector	8
		1.2.1 The Role of Shale in Energy Transition	9
		1.2.2 Shale Formations in CO_2 and H_2 Storage	9
	1.3	Wellbore Stability and Failure Mechanisms	10
		1.3.1 Role of Drilling Fluids	10
			10
		1.3.3 Stress Redistribution around a Borehole	1
		1.3.4 Sampling and Specimen Issues	12
		1.3.5 Drained vs. Undrained	12
	1.4	Roadmap of the Thesis	12
2	Ana	alytical and	
	Nui	merical Framework	4
	2.1	In-situ Stress and Effective Stress	4
		2.1.1 Far-field Stresses and Overburden	4
		2.1.2 Horizontal Stress Estimate and Calibration	15
		2.1.3 Effective Stress	15
	2.2	Analytical Solutions for a Circular Borehole	6
		2.2.1 Lamé Problem	6
		2.2.2 Kirsch Problem	6
	2.3	Mohr–Coulomb criterion recall	18
	2.4	Mud-Weight Window and Failure Criteria	18
		2.4.1 Why alternative criteria are needed in shales	19
		2.4.2 Weakness-Plane Model (WPM)	19
		2.4.3 Modified Hoek–Brown (HBm)	20
		2.4.4 Link to FLAC2D constitutive models later discussed	20
	2.5	Wellbore Trajectory vs. Far-field Stresses	20
	2.6	Poroelastic Effects	20
	2.7	Analytical—Numerical Roadmap	21
3	Tou	rnemire Shale: Data	
	and		22
	3.1	v	22
		3.1.1 Geological Context and Mineralogy	22
		v e	23
		v	23
	3.2	1	23
			24
		3.2.2 Isotropic Linear Elastic Model (ILE)	24

6	Con		56
		11	
		5.3.4 CANISO - Swapped Orientation	53
		5.3.3 CANISO - Standard Orientation	
		• •	52
		5.3.1 UBI - Standard Orientation	
	5.3	UBI and CANISO — Undrained vs Drained	
		5.2.2 CANISO, undrained: effect of far-field swap	
		5.2.1 UBI, undrained: effect of far-field swap	
	5.2	Orientation Effects: Far-field Stress Swap δ^*	
		5.1.8 Undrained Analysis	
		5.1.7 Cross-model recap and comparison	
		5.1.6 CANISO, undrained $\delta = 15^{\circ}$	
		5.1.5 CANISO, undrained $\delta = 0^{\circ}$	45
		5.1.4 Ubiquitous Joint (UBI), undrained $\delta = 15^{\circ}$	
		5.1.3 Ubiquitous Joint (UBI), undrained $\delta = 0^{\circ}$	
		5.1.2 Mohr-Coulomb (ILE-MC), undrained	
	J. <u>T</u>	5.1.1 Isotropic Linear Elastic (ILE), undrained	
_	5.1	Synthetic Cases - Undrained Conditions	
5	Res	ults and Discussions	4 0
	4.7	Note: FLAC2D - Models Hierarchies	39
	4.6	Sector B - Anomalous Tensile Zones \dots	
		4.5.2 Weak-plane-controlled (WPM, Jaeger)	
		4.5.1 Matrix-controlled Window (Mohr–Coulomb)	
	4.5	MWW Calculation	
		4.4.3 ILE vs. TIE (dry conditions)	
		4.4.2 FLAC2D Results Comparison	
	*	4.4.1 Kirsch Results	
	4.4	Validation: ILE vs. Kirsch	
	4.3	Boundary Conditions and Initial State of Stress	
	4.4	4.2.1 Mesh, Grid and Configuration	
	4.1	FLAC2D Software Overview	
	4.1	Introduction	
4		f AC2D: Implementation Validation of Models	30
	3.3	Summary and Next Steps	
		3.2.6 CANISO Model	
		3.2.5 Ubiquitous Joint Model (UBI)	
		3.2.4 Mohr-Coulomb Elastoplastic Model (ILE-MC)	
		3.2.3 Transversely Isotropic Elastic Model (TIE)	

3 Contents

List of Figures

1.1	including horizontal and vertical wells targeting shale formations. Source: U.S.	C
1.2	Energy Information Administration (2011) [4]	9
1.2	tion, and observation wells. Source: Rawaa A. Sadkhan et al. (2022) [5]	ç
1.3	Schematic representation of wellbore failure mechanisms as a function of mud pres-	
1.4	sure (source: Zhang, 2013). [9]	11 11
2.1	Schematic depth trends for total vertical stress (overburden), pore pressure (hydrostatic vs. actual) and the resulting effective vertical stress. The <i>top of overpressure</i> marks where pore pressure departs from hydrostatic. [21]	14
2.2	Schematic representation of the Lamé problem with isotropic far-field stresses σ_h (same in all directions) and mud pressure p_w from the center of the wellbore up to	
2.3	the borehole wall. The $P(r, \theta)$ indicates a generic location where stresses are calculated. Schematic representation of the Kirsch problem with anisotropic far-field stresses, shown as σ_{Hmax} (red) and σ_{hmin} (blue). Point $P(r, \theta)$ indicates a generic location	16
2.4	where the stresses are calculated	17 18
2.5	WPM strength vs. β_w : slip envelope with minimum at $45^{\circ} + \phi'_w/2$ and matrix plateau where slip is not activated. Adapted from: "An Anisotropic Failure Criterion for Jointed Rocks Under Triaxial Stress Conditions"	19
3.1	Hierarchy of constitutive models implemented in FLAC2D used in this work	24
4.1	polar mesh implemented in FLAC2D showing the grid structure: 60 radial x 60 circumferential zones	31
4.2	Orientation of far-field stresses in the numerical model; $\sigma_{Hmax} = 30 \ MPa$ acts along the x-axis, while $\sigma_{hmin} = 20 \ MPa$ acts along the y-axis. The wellbore	9.0
4.3	axis is perpendicular to the page	32 34
4.4	Sector B (θ =90°): FLAC2D vs. Kirsch trends for hoop and radial stresses	
4.5	Radial profile of σ_r and σ_θ in A $(\theta = 0^\circ)$: ILE vs TIE, dry, $p_w = 0$	
4.6	Radial profile of σ_r and σ_θ in B ($\theta = 90^\circ$): ILE vs TIE, dry, $p_w = 0$	35
4.7	Tension/compression anomalies	38
5.1	ILE undrained, radial profiles of total stresses σ_{θ} (red) and σ_{r} (blue)	41

5.2	ILE undrained tension/compression map	41
5.3	MC undrained - tension/compression map	42
5.4	MC undrained — state map. Narrow lobes at the wall (B direction) show At Yield	
	in Shear or Vol. and Elastic, Yield in Past. The latter means that yielding occurred	
	during the numerical convergence and the zone is elastic at the end of the step	42
5.5	UBI undrained — tension/compression map for $\delta=0^{\circ}$	43
5.6	UBI undrained — state map for $\delta = 0^{\circ}$	44
5.7	UBI undrained — state map for $\delta=15^{\circ}$	45
5.8	CANISO undrained — state map for $\delta=0^{\circ}$	45
5.9	CANISO undrained — state map for $\delta=15^{\circ}$	46
5.11	Undrained pore-pressure fields ($p_f = 11$ MPa, $p_w = 14$ MPa)	48
5.12	Undrained pore pressure with tilted bedding. Lobes rotate and become slightly	
	asymmetric ($\delta = 15^{\circ}$)	48
5.13	Far-field stresses swap	49
5.14	UBI — state map: undrained, effect of far-field swap at $\delta=0^{\circ}$	49
5.15	UBI — state map: undrained, effect of far-field swap at $\delta=15^{\circ}$	50
5.16	CANISO — state map: undrained, effect of far-field swap at $\delta=0^{\circ}$	50
	CANISO — state map: undrained, effect of far-field swap at $\delta=15^{\circ}$	
5.18	UBI — state map: undrained vs drained at $\delta = 0^{\circ}$	52
5.19	UBI — state map: swapped undrained vs drained at $\delta^* = 0^{\circ}$	52
5.20	CANISO — state map: undrained vs drained at $\delta = 0^{\circ}$	53
5.21	CANISO — state map: swapped undrained vs drained at $\delta^* = 0^\circ$, $p_w = 12.5$ MPa	54
5.22	CANISO – Tension/compression map, swapped UNDRAINED case at $\delta^* = 0^{\circ}$, $p_w =$	
	12.5 MPa	54

List of Tables

2.1	FLAC2D constitutive models and corresponding analytical solutions	20
3.1	Typical mineralogical composition of Tournemire shale	22
3.2	ILE dry model parameters for dry conditions	
	ILE undrained model parameters	
3.4	TIE model parameters in FLAC2D	25
3.5	Mohr-Coulomb model parameters in FLAC2D	
3.6	Ubiquitous Joint model parameters	27
3.7	CANISO model parameters	27
4.1	Mesh parameters for polar grid generation	31
4.2	Boundary conditions and initial stress state	
4.3	Tension/Compression Maps Legend	
4.4	Mesh parameters for polar grid generation	39
4.5	gratio tuning	
5.1	Synthetic case inputs	40

Introduction

1.1 Overview

Drilling operations are generally considered demanding, not only in terms of effort but also in geological expertise, most of the difficulty arises when passing through shale layers, which pose a significant challenge for drilling and, more broadly, for the global energy sector. Shale's mechanical behavior is highly complex, characterized by strong heterogeneity (including layers and laminations), pronounced anisotropy (with different stiffness and strength along versus across bedding planes), and extremely low permeability. These intrinsic properties, as we will see, make drilling challenging and make it difficult to predict when and where failures will occur. Consequently, wellbore instability in shale is a primary operational problem. Small errors in mud weight or in-situ stress estimates often lead to large and costly failures. Unpredictable fracture behavior and sudden pressure changes further emphasize the need for a robust geomechanical characterization to mitigate risk. Borehole failures alone are estimated to cause over one billion USD in annual losses and account for more than 40% of all drilling interruptions. This highlights how widespread and economically critical these instabilities are [1, 2]. This Thesis addresses these complexities by focusing on a comparative analysis of constitutive models for drilling anisotropic Tournemire Shale, using numerical calculations in FLAC2D 8.1.

1.2 Shale Geomechanics in a Transitioning Energy Sector

As anticipated before, shale geomechanics remains crucial even as the energy landscape shifts. Although the oil & gas industry is expected to gradually shrink, drilling operations for underground fluid storage won't disappear and will still demand expert attention. The physical behavior of shale doesn't change just because its purpose does: whether the goal is hydrocarbon extraction, carbon dioxide sequestration, or hydrogen storage, engineers must still understand how these layered rocks deform and fail when penetrated by a well. In the following subsections we will see that shale formations, while once mainly associated with gas production, are now tied to the broader energy transition. Their role as a "bridge fuel" highlights how shale gas temporarily reshaped energy markets by providing a lower-carbon option compared to coal or oil. The rapid development of shale gas in North America also marked a scientific turning point, as the difficulties in drilling these reservoirs revealed the complexity of shale geomechanics and issues such as wellbore instability, fracture propagation, and fluid loss. These lessons now provide the basis for new applications, from CO_2 to H_2 storage, where integrity and long-term stability are paramount.

1.2.1 The Role of Shale in Energy Transition

Over the past few decades, shale gas has played a central role in the global energy transition, often described as a "bridge fuel" that helps move the world away from traditional fossil fuels toward more sustainable energy sources. Shale gas emits considerably less CO_2 per unit of energy compared to coal or oil, thus a relatively lower carbon footprint. Its large-scale development, particularly in North America, has been a key factor in reducing emissions from the power sector by replacing older and more polluting fuel sources [3].

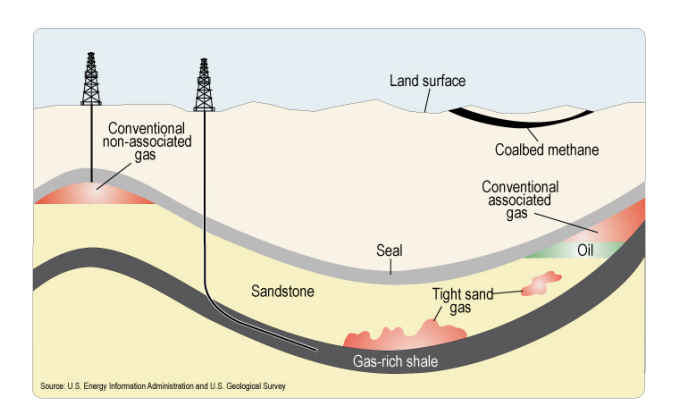


Figure 1.1: Schematic showing different types of petroleum accumulations and development, including horizontal and vertical wells targeting shale formations. Source: U.S. Energy Information Administration (2011) [4].

Understanding this role also helps explain why shale mechanics continues to attract attention: safe and predictable drilling is not only about short-term production, but also about ensuring that these wells operate with minimal environmental and economic risks. This bridge function, as we will see, marks only the first chapter in a broader story where shale continues to matter for the subsurface of tomorrow.

1.2.2 Shale Formations in CO_2 and H_2 Storage

At the same time, shale formations are becoming increasingly important for other energy-related applications. As the push to decarbonize our energy systems grows stronger, solutions like carbon dioxide (CO_2) and hydrogen (H_2) storage are quickly catching on.

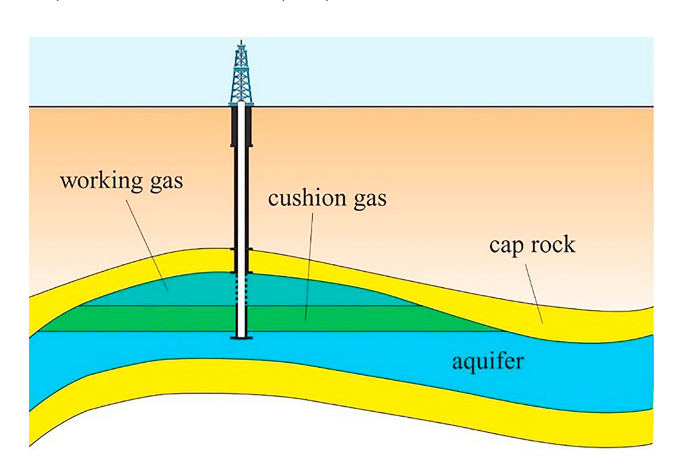


Figure 1.2: Schematic of hydrogen storage in a depleted gas reservoir, showing injection, extraction, and observation wells. Source: Rawaa A. Sadkhan et al. (2022) [5].

Many of these projects require drilling wells that pass through shale layers, where the formations often act as natural seals or barriers underground for underground reservoirs.

Shale's structural properties make it critical for maintaining the integrity of the storage-site over long timescales [6, 7]. Ensuring wellbore stability in such settings is therefore essential not only to prevent leakage, but also to guarantee the reliability and safety of fluid storage. [8]. In other words, the challenges that once tested drilling engineers now play a decisive role in society's capacity to safely store energy and contain greenhouse gases. What was previously recognized as a technical or operational issue is today a fundamental pillar of the ongoing energy transition.

Hence, shale mechanics is a center of gravity for these new applications, but the most interesting concern, not only for this thesis work, remains the wellbore stability. In the following sections, we are going to review the main failure mechanisms and how they affect wellbore integrity.

1.3 Wellbore Stability and Failure Mechanisms

Wellbore stability is a central topic in most geomechanics studies and refers to the ability of a borehole to maintain its structural integrity both during drilling and once the excavation is completed. In practical terms, this means that the surrounding rock must be able to withstand the redistribution of in situ stresses and the pressure exerted by the drilling fluid without failing.

1.3.1 Role of Drilling Fluids

Drilling fluids play a dual role in wellbore stability. They not only transport drill cuttings to the surface and cool the bit, but also provide a counterbalancing pressure that helps prevent collapse or fluid influx. In practice, the mud weight P_w is the main controllable parameter available to drilling engineers to keep the borehole stable. As later chapters will show, the safe range of P_w is constrained by both shear and tensile failure limits, defining the so-called Mud Weight Window (MWW). A wrong diagnosis of the instability mechanism can result in an inappropriate mud weight adjustment, which may further destabilize the borehole.

1.3.2 Failure Types and Mud Weight Window

In geomechanics, the wellbore stability is primarily important. The wellbore can be defined as "stable" only if the rock continues to fulfill its engineering function, that is to say, resisting compressive loadings (i.e. shear failure, breakouts or slip along weakness planes) and tensile loadings (i.e. tensile failure, hydraulic fracturing). In essence, to stay away from failure, the driller must keep the mud pressure in a safe range called "Mud Weight Window" (MWW).

Failure can occur in two main forms:

- Shear failure which appears in the form of borehole collapse, breakout, or slippage along pre-existing weak planes (e.g., bedding planes in shale).
- Tensile failure more commonly referred to as hydraulic fracturing, which occurs when the fluid pressure inside the borehole exceeds the tensile strength of the surrounding rock.

Fig. 1.3 illustrates how mud pressure influences the mechanical response of the borehole. Mud pressure (or mud weight) plays a central role in this balance, as summarized in Eq. 1.1.

$$\begin{cases} P_w = P_{fo} & \text{(drilling in balance)} \\ P_w < P_{fo} & \text{(drilling in underbalance)} \\ P_w > P_{fo} & \text{(drilling in overbalance)} \end{cases}$$
(1.1)

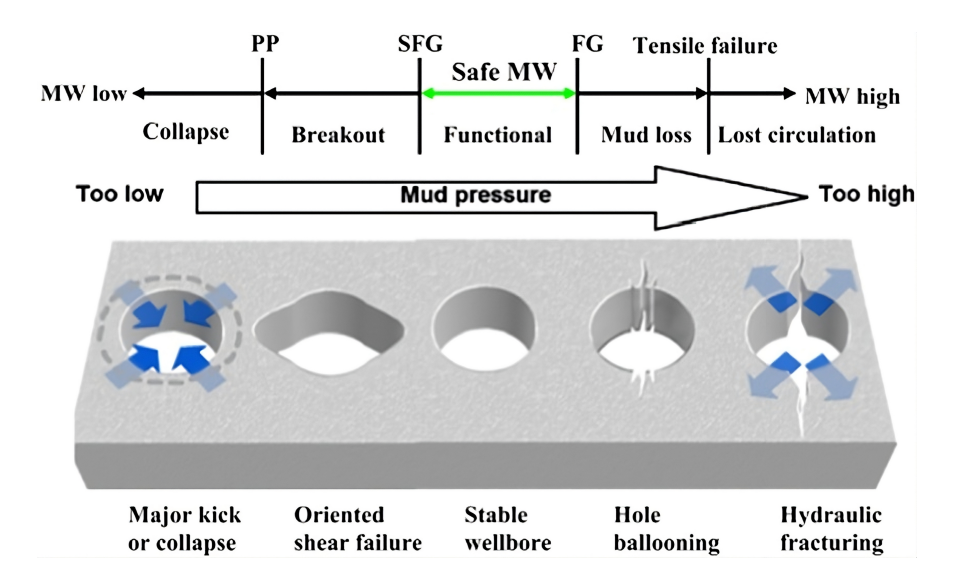


Figure 1.3: Schematic representation of wellbore failure mechanisms as a function of mud pressure (source: Zhang, 2013). [9]

If the mud pressure is too low (underbalanced), the rock around the borehole cannot withstand the in situ stresses, and the risk of collapse or breakout increases significantly. On the other hand, if the mud pressure is too high (overbalanced), it may exceed the tensile strength of the rock, leading to hydraulic fracturing and possible fluid losses. For this reason, the mud pressure must be kept within a safe range, commonly referred to as the **Mud Weight Window (MWW)**, as defined in Eq. 1.3.

$$P_{w,\text{min}}$$
 (to avoid shear failure), $P_{w,\text{max}}^{\text{frac}}$ (to prevent tensile failure). (1.2)

$$P_{w,\min} \le P_w \le P_{w,\max}^{\text{frac}}.$$
 (1.3)

1.3.3 Stress Redistribution around a Borehole

Drilling a borehole alters the equilibrium of the in situ stress field. Once the rock is removed, the borehole wall is supported only by the drilling fluid pressure, which rarely matches the original stresses.

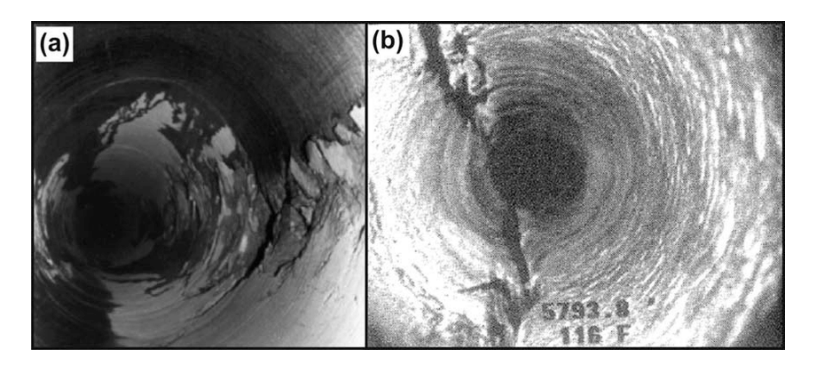


Figure 1.4: Examples of stress-induced borehole instabilities observed with a downhole camera: (a) borehole breakout due to compressive shear failure; (b) drilling-induced fracture caused by tensile failure. Source: Asquith and Krygowski (2004) and Tingay et al. (2008). [10, 11]

As a result, the surrounding formation undergoes a redistribution of stresses, often leading to local concentrations that exceed the initial in situ values. This phenomenon is a primary cause of wellbore instabilities and highlights why stress analysis is fundamental in drilling engineering, Fig. 1.4 shows both breakout and hydraulic fracturing in a wellbore.

1.3.4 Sampling and Specimen Issues

Testing shale in the laboratory presents difficulties because coring, depressurization, and trimming can disturb the rock and alter its pore conditions. As a result, measured strength and stiffness can be lower than in situ values. Laboratory work is still essential, but procedures should reduce disturbance and consider anisotropy [12]. The fluid environment also matters: porous rocks are often much weaker when water-saturated, so when outcrop samples are used as substitutes the test conditions must be realistic [13]. A practical approach is to combine preserved cores with well logs to calibrate elastic and poroelastic parameters. The effect of mud and other fluids on shale strength can be observed at core or micro-sample scale and should be included in log interpretation [14]. When cores are few or of low quality, rock mechanical properties can be estimated from formation evaluation logs using established methods [15]. Because shale is layered, it does not behave the same in all directions. Properties such as Young's modulus, shear strength and permeability change with the angle to bedding; the rock is often stiffer and stronger along bedding than across it. These directional effects influence wellbore stability. Pore pressure and temperature can also change the response over time, especially when drilling fluids interact with the formation. This thesis first focuses on directional effects (anisotropy), then discusses fluid-related changes when comparing undrained and drained cases.

For these reasons, this thesis uses published datasets and an analytical and numerical workflow rather than relying only on laboratory tests. This topic will be taken up again and discussed in more detail in Chapter 3, *Tournemire Shale Data and Parameterization*.

1.3.5 Drained vs. Undrained

Shale has very low permeability, so just after drilling the rock behaves in an undrained way. Stress changes are faster than pore fluid can move, so pore pressure rises temporarily and reduces the effective stress that holds the grains together [16, 17]. This mechanism is known as the *Skempton effect*. The pore pressure change Δu is linked to the mean total stress change $\Delta \sigma$ by the Skempton coefficient B:

$$\Delta u = B \,\Delta \sigma \tag{1.4}$$

The coefficient B varies between 0 and 1. A value close to 1 means that most of the applied stress is transferred into pore pressure, which is typical for saturated clays and mudstones. In rocks with lower porosity or partial saturation, B is smaller. Typical values are $B \approx 0.99$ for clays, 0.83 for mudstones, and much lower for dense rocks like limestone or basalt [18]. When B is high, effective stresses drop quickly, which makes the near-wellbore region prone to breakouts or tensile failure [16].

Over longer times, pore fluids can diffuse and the system moves to a drained response, where excess pore pressures vanish and the stress state changes again [19, 20]. Both undrained and drained cases are important for wellbore stability: the first controls short-term failure during drilling, the second controls long-term integrity. The role of the Skempton coefficient B and the related Biot coefficient α will be explained in more detail in Chapter 2, together with the analytical framework.

1.4 Roadmap of the Thesis

This chapter explained why shale formations challenge wellbore stability and why both short-term (undrained) and long-term (drained) responses matter. Chapter 2 presents the analytical and numerical framework. It reviews the elastic solutions of Lamé and Kirsch and the

constitutive models for shale, including transverse isotropy and weakness planes, which we use for validation. Chapter 3 compiles the Tournemire shale dataset from published sources and explains parameter choices with respect to bedding orientation. Chapter 4 describes the FLAC2D modelling setup, including mesh, boundary conditions and the implementation of constitutive laws for drained and undrained cases. Chapter 5 reports the results, compares analytical and numerical predictions in isotropic and anisotropic settings and studies the effect of far-field stress orientation on the mud-weight window. Chapter 6 gives the main conclusions and recommendations for engineering practice and future work. This path, from analytical background to numerical validation and application, keeps the study rigorous and useful for operations.

Analytical and Numerical Framework

2.1 In-situ Stress and Effective Stress

2.1.1 Far-field Stresses and Overburden

In geomechanics the far-field state of stress is described by one vertical stress, two horizontal stresses, and the pore pressure. In the literature the vertical axis is taken *positive downward*. Vertical equilibrium in a homogeneous column gives:

$$\frac{\partial \sigma_z}{\partial z} - \gamma = 0 \quad \Rightarrow \quad \sigma_v(z) = \gamma z, \tag{2.1}$$

where γ is the unit weight of the overburden. Sediment bulk density in the overburden typically ranges $1.8-2.2\,\mathrm{g\,cm^{-3}}$; as a rule of thumb the vertical stress increases with depth at about $20\,\mathrm{MPa\,km^{-1}}$.

Under hydrostatic conditions the pore pressure at depth z is:

$$u(z) = \gamma_w z, \tag{2.2}$$

where γ_w is the unit weight of the pore fluid; for seawater brine the density is $\rho_w \approx 1.03 - 1.07 \,\mathrm{g\,cm^{-3}}$. In many basins the pore pressure deviates from the hydrostatic trend (overpressure or underpressure), which directly impacts stability because it changes the effective stress, as shown in Fig. 2.1

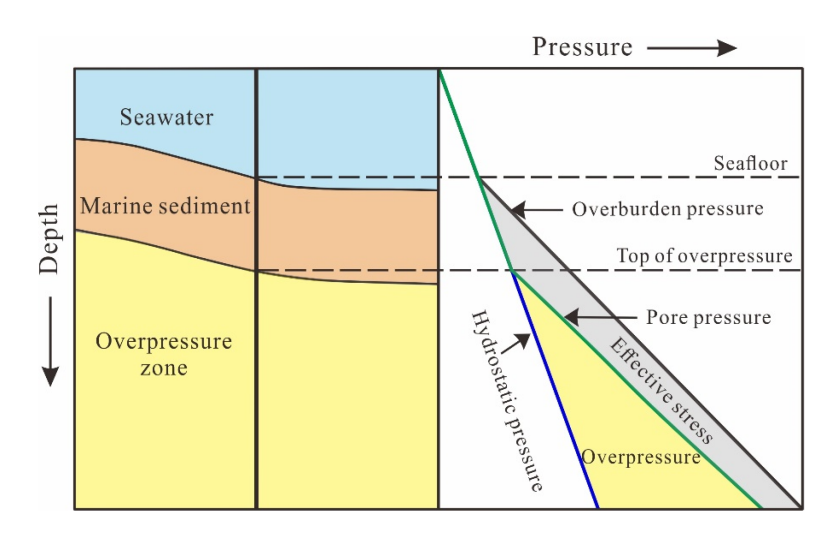


Figure 2.1: Schematic depth trends for total vertical stress (overburden), pore pressure (hydrostatic vs. actual) and the resulting effective vertical stress. The *top of overpressure* marks where pore pressure departs from hydrostatic. [21]

The horizontal stresses cannot be obtained from static equilibrium alone, because their actual magnitude depends on boundary conditions and on the geologic stress history of the deposits. In a laterally uniform medium, with no significant body forces in the x-direction, the horizontal equilibrium does not uniquely determine the stress; it only gives

$$\frac{\partial \sigma_x}{\partial x} + \frac{\partial \tau_{xz}}{\partial z} + \frac{\partial \tau_{xy}}{\partial y} = 0, \implies \frac{\partial \sigma_x}{\partial x} = 0.$$
 (2.3)

This tells us that σ_x is nearly constant laterally, but it does not give its *value*. Therefore, a practical first estimate is the at–rest model:

$$\sigma'_h = K_0 \, \sigma'_v, \qquad \sigma_h = \sigma'_h + \alpha \, u,$$
 (2.4)

Since K_0 is not unique and can vary widely with depth, to set reasonable thresholds we use the bounds in Eq. (2.5), which include the friction angle ϕ' and provide lower and upper limits:

$$\frac{1 - \sin \phi'}{1 + \sin \phi'} \le K_0 \le \frac{1 + \sin \phi'}{1 - \sin \phi'}.$$
 (2.5)

2.1.2 Horizontal Stress Estimate and Calibration

In practice, K_0 provides a first estimate of the *effective* horizontal stress, $\sigma'_h = K_0 \sigma'_v$. Field measurements (mini-frac/LOT, image logs, caliper) are then used to calibrate K_0 and to separate the two components σ_H and σ_h . This estimate is essential for wellbore stability analyses, since the horizontal stresses largely control breakout and fracture phenomena.

2.1.3 Effective Stress

The stress field in porous rocks is usually described within the framework of linear poroelasticity, which generalizes Hooke's law by including the effect of pore pressure in fluid–saturated media. In this formulation, the total stress tensor σ_{ij} is decomposed into the effective stress σ'_{ij} , carried by the solid skeleton, and the contribution of the pore pressure u according to the Terzaghi–Biot relation:

$$\sigma'_{ij} = \sigma_{ij} - \alpha u \, \delta_{ij}, \tag{2.6}$$

where α is the Biot coefficient ($0 \le \alpha \le 1$), and δ_{ij} is the Kronecker delta. This principle was first stated by Terzaghi (1936), who argued that all measurable deformations depend on effective stress alone, and was later generalized by Biot (1941, 1955) within this theoretical setting. The vertical component reduces to:

$$\sigma_v' = \sigma_v - \alpha u. \tag{2.7}$$

The coefficient α reflects the compressibility contrast between the rock frame and the mineral grains; in isotropic form one may write:

$$\alpha = 1 - \frac{K'}{K_s},\tag{2.8}$$

with K' the drained bulk modulus of the skeleton and K_s the bulk modulus of the solid grains. Shales typically exhibit high α (often close to 1), so changes in u are nearly proportional to changes in σ' . Equations (2.6)–(2.7) provide the basis for total stresses into effective quantities, later used in the Lamé–Kirsch solutions and in the drained/undrained analyses.

2.2 Analytical Solutions for a Circular Borehole

In this section we are going to present the analytical solutions for a circular borehole with a radius $r = R_w$. In particular, in this thesis work, we considered a vertical wellbore drilled in an anisotropic far-field stress field (i.e. shale formations). The considered reference values are $\sigma_{Hmax} = 30$ MPa, $\sigma_{hmin} = 20$ MPa and $\sigma_z = \sigma_{axis} = 25$ MPa. For the sake of clarity, we first introduce the simplest analytical solution, also known as "Lamé", which considers an isotropic and homogeneous rock, where $\sigma_{Hmax} = \sigma_{hmin}$. Even though it represents an ideal case, it provides a clear and useful baseline to understand how stresses redistribute around the well. Then, the "Kirsch" analytical solution will be presented, which increases the complexity level of the Lamé model, accounting for horizontal anisotropic far-field stresses.

Thereafter, the failure mechanism will be explained to give a broader understanding, not only of the geomechanics framework that is embedded in the numerical models, but also about the MWW calculations that we will see in chapter 4.

2.2.1 Lamé Problem

The Lamé problem is the simplest analytical solution in an infinite isotropic elastic medium with equal horizontal stresses. The well is vertical and aligned with the overburden. Despite its simplicity, it gives a clear baseline to understand how mud pressure p_w replaces the removed rock and redistributes stresses around the borehole.

The general solution for the total stresses in cylindrical coordinates is given by [22]:

$$\sigma_r = \sigma_h \left(1 - \frac{R_w^2}{r^2} \right) + p_w \frac{R_w^2}{r^2}$$
 (2.9)

$$\sigma_{\theta} = \sigma_h \left(1 + \frac{R_w^2}{r^2} \right) - p_w \frac{R_w^2}{r^2}$$
 (2.10)

$$\sigma_{axis} = \sigma_z = \sigma_v, \qquad \tau_{r\theta} = \tau_{z\theta} = \tau_{zr} = 0 \quad (2.11)$$

where R_w is the borehole radius, r the radial distance from the center, σ_r the radial stress, σ_θ the tangential stress, and σ_z the vertical stress. At the borehole wall $(r = R_w)$, these equations reduce to:

$$\sigma_r = p_w, \qquad \sigma_\theta = 2\sigma_h - p_w, \qquad \sigma_z = \sigma_v \quad (2.12)$$

This result shows that the radial stress equals the mud pressure, while the tangential stress can reach values up to twice the far-field horizontal stress minus the mud pressure. This concentration of tangential stress, typical of the Lamé solution, highlights why boreholes are particularly sensitive to even small variations in mud weight.

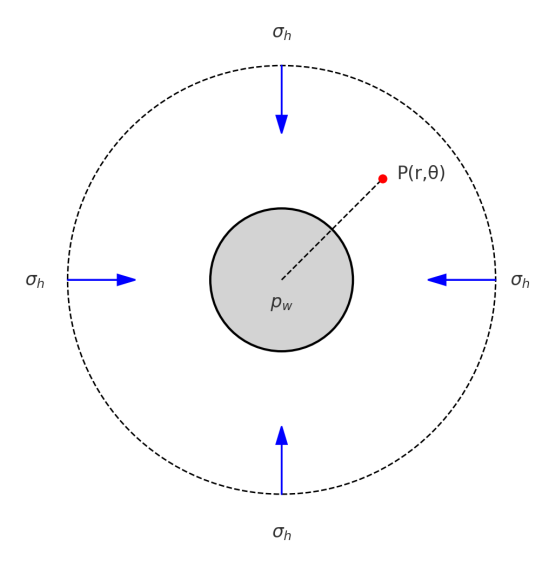


Figure 2.2: Schematic representation of the Lamé problem with isotropic far-field stresses σ_h (same in all directions) and mud pressure p_w from the center of the wellbore up to the borehole wall. The $P(r,\theta)$ indicates a generic location where stresses are calculated.

2.2.2 Kirsch Problem

We stay within isotropic linear elastic (ILE) and plane—strain assumptions. The Kirsch problem extends the Lamé solution to anisotropic horizontal far-field stresses ($\sigma_{Hmax} \neq \sigma_{hmin}$).

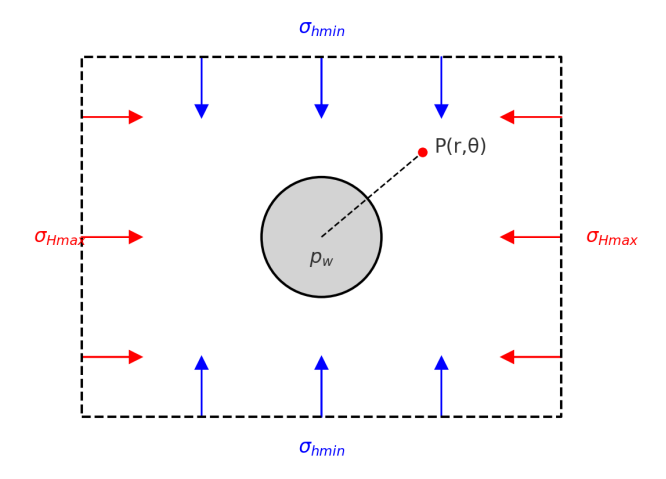


Figure 2.3: Schematic representation of the Kirsch problem with anisotropic far-field stresses, shown as σ_{Hmax} (red) and σ_{hmin} (blue). Point $P(r,\theta)$ indicates a generic location where the stresses are calculated.

The classical Kirsch solution gives the *total* stresses in cylindrical coordinates at any point $P(r, \theta)$ outside the borehole wall [22]:

$$\sigma_{r} = \frac{1}{2} (\sigma_{Hmax} + \sigma_{hmin}) \left(1 - \frac{R_{w}^{2}}{r^{2}} \right) +$$

$$+ \frac{1}{2} (\sigma_{Hmax} - \sigma_{hmin}) \left(1 - \frac{4R_{w}^{2}}{r^{2}} + \frac{3R_{w}^{4}}{r^{4}} \right) \cos 2\theta + p_{w} \frac{R_{w}^{2}}{r^{2}}.$$
(2.13)

$$\sigma_{\theta} = \frac{1}{2} \left(\sigma_{Hmax} + \sigma_{hmin} \right) \left(1 + \frac{R_w^2}{r^2} \right) - \frac{1}{2} \left(\sigma_{Hmax} - \sigma_{hmin} \right) \left(1 + \frac{3R_w^4}{r^4} \right) \cos 2\theta - p_w \frac{R_w^2}{r^2}. \tag{2.14}$$

$$\tau_{r\theta} = -\frac{1}{2}(\sigma_{Hmax} - \sigma_{hmin}) \left(1 + \frac{2R_w^2}{r^2} - \frac{3R_w^4}{r^4} \right) \sin 2\theta.$$
 (2.15)

$$\sigma_z = \sigma_v - 2\nu \left(\sigma_{Hmax} - \sigma_{hmin}\right) \frac{R_w^2}{r^2} \cos 2\theta, \qquad \tau_{rz} = \tau_{\theta z} = 0. \tag{2.16}$$

Note. These are total stresses. For failure checks we convert to effective stresses using $\sigma'_{ij} = \sigma_{ij} - \alpha u \, \delta_{ij}$ (Section 2.1).

At the borehole wall $(r = R_w)$, the radial stress is equal to the mud pressure $(\sigma_r = p_w)$, while the tangential and axial stresses depend on the azimuthal angle θ . In particular, the analytical solutions simplify at the two principal directions, $\theta = 0^{\circ}$ and $\theta = 90^{\circ}$ are:

• At Point A ($\theta = 0^{\circ}$, direction of σ_{Hmax}):

$$\sigma_r = p_w, \qquad \sigma_\theta = 3\sigma_{hmin} - \sigma_{Hmax} - p_w, \qquad \sigma_z = \sigma_v - 2\nu(\sigma_{Hmax} - \sigma_{hmin})$$

• At Point B ($\theta = 90^{\circ}$, direction of σ_{hmin}):

$$\sigma_r = p_w, \qquad \sigma_\theta = 3\sigma_{Hmax} - \sigma_{hmin} - p_w, \qquad \sigma_z = \sigma_v + 2\nu(\sigma_{Hmax} - \sigma_{hmin})$$

These expressions are obtained by evaluating Eqs. (2.13)–(2.16) at $r=R_w$ and substituting $\cos 2\theta$, $\sin 2\theta$ for $\theta=0^\circ,90^\circ$.

2.3 Mohr–Coulomb criterion recall

We adopt the linear Mohr–Coulomb (M–C) criterion in effective stresses. In the shear–normal plane,

$$\tau_s = c' + \sigma'_n \tan \phi',$$

which is equivalent, in principal stresses, to

$$\sigma_1' = C_0 + N_\phi \, \sigma_3', \qquad C_0 = \frac{2c'\cos\phi'}{1-\sin\phi'}, \quad N_\phi = \frac{1+\sin\phi'}{1-\sin\phi'}.$$

It follows that UCS = C_0 and UTS = $T_0 = \frac{2c'\cos\phi'}{1+\sin\phi'}$; the intact failure plane is inclined by $\beta = 45^{\circ} + \phi'/2$. M–C is linear and ignores σ'_2 , but it provides a clear baseline in order to compute the MWW bounds.

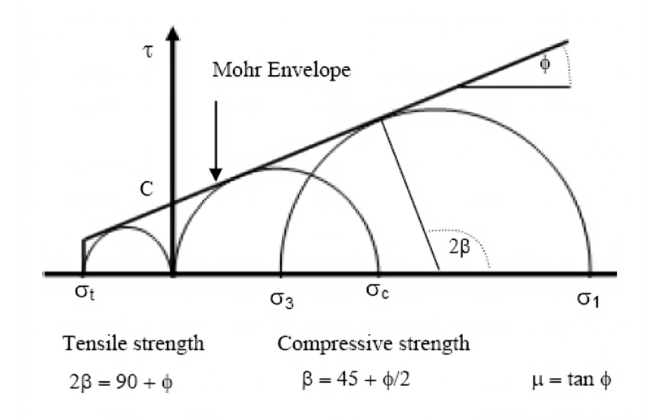


Figure 2.4: Mohr-Coulomb envelope in effective stresses with tensile cutoff $T_0 = \sigma_t$. Failure occurs when the Mohr circle for (σ'_3, σ'_1) is tangent to the line; $\beta = 45^{\circ} + \phi'/2$. adapted from "Failure criteria development using triaxial test multistage and conventional"

2.4 Mud-Weight Window and Failure Criteria

The analytical stress solutions (Lamé/Kirsch) become useful for wellbore stability once they are combined with a failure criterion. This allows us to estimate the safe range of mud pressure p_w : a lower limit to prevent shear collapse, and an upper limit to prevent tensile fractures induced by drilling. In the following, all calculations are expressed in terms of effective stresses.

Wall stresses in compact form. At the borehole wall the effective stresses can be written as

$$\sigma'_{\theta} = S - p_w - p_f, \qquad \sigma'_r = p_w - p_f, \qquad \sigma'_z = S_z - p_f,$$

with

$$S = \sigma_{Hmax} + \sigma_{hmin} - 2(\sigma_{Hmax} - \sigma_{hmin})\cos 2\theta, \quad S_z = \sigma_v - 2\nu(\sigma_{Hmax} - \sigma_{hmin})\cos 2\theta.$$

We will use these shorthand forms in the mud-weight bounds. In order to estimate the shear-collapse bound $p_{w,min}$, which expresses the minimum mud pressure required to avoid shear failure, we check two possible scenarios:

$$\sigma'_{\theta} > \sigma'_{z} > \sigma'_{r}$$
 and $\sigma'_{z} > \sigma'_{\theta} > \sigma'_{r}$

The Mohr–Coulomb (MC) failure condition is then applied for each of the 2 cases, depending on whether σ'_{θ} or σ'_{Z} is the maximum effective stress.

$$\sigma_1' = C_0 + N_\phi \, \sigma_3', \qquad C_0 = \frac{2c'\cos\phi'}{1-\sin\phi'}, \quad N_\phi = \frac{1+\sin\phi'}{1-\sin\phi'}.$$

This yields the two candidates, obtained by substitution:

$$p_{w,\min}^{(\theta>z)} = \frac{S - C_0 + (N_\phi - 1) p_f}{1 + N_\phi}, \tag{2.17}$$

$$p_{w,\min}^{(z>\theta)} = \frac{S_z - C_0 + (N_\phi - 1) \, p_f}{N_\phi}.$$
 (2.18)

The true lower bound is $p_{w,\min} = \max\{p_{w,\min}^{(\theta>z)}, p_{w,\min}^{(z>\theta)}\}$. For tensile failure we impose $\sigma_3' = -T_0$. Along principal directions this gives

$$p_{w,\max} = S - p_f + T_0, \tag{2.19}$$

whose minimum with respect to θ occurs at $\theta = 0^{\circ}$ (point A), where $S = 3\sigma_{hmin} - \sigma_{Hmax}$. Hence

$$p_{w,\text{max}}^{(\text{fracture, A})} = 3\sigma_{hmin} - \sigma_{Hmax} - p_f + T_0.$$
(2.20)

2.4.1 Why alternative criteria are needed in shales

Rock failure is often treated as isotropic, but many rocks—especially shales—are *transversely isotropic* because of parallel weakness planes. Their strength is lower along those planes, and the criterion must account for *orientation*.

2.4.2 Weakness-Plane Model (WPM).

WPM considers slip on planes at inclination β_w :

$$(\sigma_1' - \sigma_3')_{\text{slip}} = \frac{2 \cdot (c_w' + \sigma_3' \tan \phi_w')}{1 - \frac{\tan \phi_w'}{\tan \beta_w} \cdot \sin 2\beta_w}.$$
(2.21)

It predicts a minimum strength at $\beta_w = 45^{\circ} + \phi'_w/2$. For β_w near 0° or 90° slip cannot occur and the main failure mode is dictated by the *matrix plateau*, which follows again Mohr–Coulomb criterion with parameters (c', ϕ') . In practice, for each azimuth θ we evaluate both (2.21) and MC (for the matrix) in order to have a clear reference pressure value.

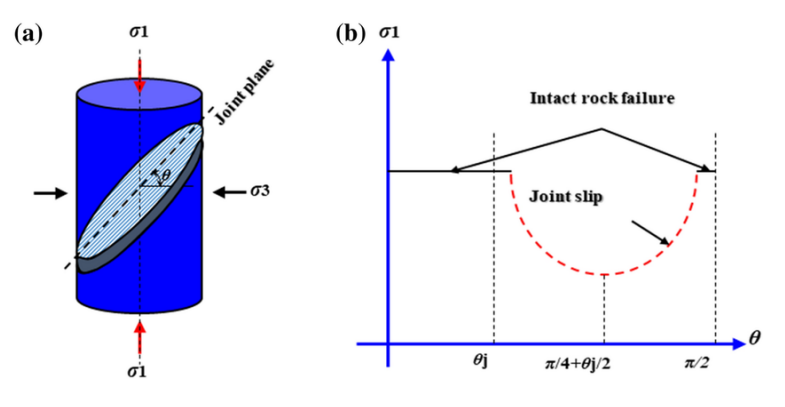


Figure 2.5: WPM strength vs. β_w : slip envelope with minimum at $45^{\circ} + \phi'_w/2$ and matrix plateau where slip is not activated. Adapted from: "An Anisotropic Failure Criterion for Jointed Rocks Under Triaxial Stress Conditions"

2.4.3 Modified Hoek–Brown (HBm).

The modified Hoek-Brown model is an empirical, non-linear formula that fits triaxial test data better, especially with low confinement and is widely used for anisotropic rocks:

$$\sigma_1' = \sigma_3' + \sigma_{c,\beta_w} \left(m_{\beta_w} \frac{\sigma_3'}{\sigma_{c,\beta_w}} + s_{\beta_w} \right)^{a_{\beta_w}},$$

where $\sigma_{c,\beta_w}, m_{\beta_w}, s_{\beta_w}, a_{\beta_w}$ vary with the weakness-plane inclination β_w .

2.4.4 Link to FLAC2D constitutive models later discussed

The analytical solutions and failure criteria presented in the previous sections provide the theoretical background for wellbore stability analysis, yet shales exhibit complex behavior that often requires numerical modeling to be completely understood. In this section, we bridge the gap between the analytical theory we have seen and numerical implementation by linking each constitutive model used in FLAC2D with failure criteria. What has been said is reported in the Table 2.1 below:

FLAC2D Model	Elastic Behavior	Failure Mechanism	Analytical Reference
ILE	Isotropic	None (elastic only)	Kirsch solution (validation)
TIE	Transversely isotropic	None (elastic only)	Modified Kirsch for anisotropy
ILE-MC	Isotropic	Mohr-Coulomb yield	Kirsch + MC criterion
UBI	Isotropic	$egin{array}{lll} { m MC & matrix} & + & { m weak} \ { m plane} \end{array}$	${ m Kirsch} + { m WPM/MC}$
CANISO	Transversely isotropic	Weak plane slip/tension	Anisotropic solution + WPM

Table 2.1: FLAC2D constitutive models and corresponding analytical solutions.

2.5 Wellbore Trajectory vs. Far-field Stresses

The orientation of a borehole with respect to the in-situ stresses has a first-order impact on stability. A vertical well is aligned with the vertical principal stress σ_v (which may be σ_1 , σ_2 or σ_3 depending on the stress regime). When the horizontal stresses are equal $(\sigma_{Hmax} = \sigma_{hmin})$, the redistribution around a vertical hole is axisymmetric (Lamé). If $\sigma_{Hmax} \neq \sigma_{hmin}$, the stress concentration follows the Kirsch pattern with two critical azimuths (A and B), which control breakout and hydraulic fracture directions. Inclined and horizontal wells intersect the stress tensor at different angles and usually amplify these effects in transversely isotropic shales.

2.6 Poroelastic Effects

During drilling operation times, the pore fluid behavior of shale is mostly undrained, since the low permeability does not allow the formation to drain out the pore spaces in that time window. Hence, a rapid pore-pressure change is observed Δu and it is governed by Skempton's coefficient B. This effect reduces the effective stresses $(\Delta \sigma' = \Delta \sigma - \alpha \Delta u)$ locally and may trigger early shear or tensile failure. As time goes by, the formation behavior shifts to drained conditions; this could alter the MWW and induce failure. This phenomenon and the

differences between undrained and drained conditions will be discussed later, in chapter 5 related to the results discussion, with a model comparison.

2.7 Analytical-Numerical Roadmap

Lamé and Kirsch provide the baseline stress field used to compute mud-weight bounds with Mohr–Coulomb (and, for anisotropy, WPM/HBm). In Chapter 4 we compare these analytical predictions with FLAC2D (v8.1) simulations for: (i) drained elastic cases (ILE, TIE), (ii) undrained elastic and elasto-plastic cases (ILE-UNDRAINED, ILE-MC-UNDRAINED), and (iii) anisotropic formulations with weakness planes (UBI, CANISO). Case studies on the Tournemire Shale then show when the analytical bounds hold and when full numerical modelling is required.

Tournemire Shale: Data and Constitutive Models

3.1 Data Sources and Objectives

This chapter presents the geomechanical data used in this thesis work; The main goal is to provide a consistent dataset and allow for a fair comparison between the various constitutive models. Moreover, this study must be reproducible and allow readers to properly evaluate the results shown later. The data for Tournemire shale come from laboratory tests reported by Abdi et al. (2015) [23], who performed uniaxial, triaxial and Brazilian tests on Tournemire shale samples. These test results will serve as input for the various constitutive models in FLAC2D, ensuring our numerical simulations are as case-specific as possible.

3.1.1 Geological Context and Mineralogy

The Tournemire shale is a Toarcian-age argillaceous formation located in southern France. It has been extensively studied as an analogue for clay-rich cap rocks due to its:

- Low permeability
- Strong bedding-induced anisotropy
- Well-preserved mineralogical composition
- Accessibility through underground research laboratory

Understanding the mineralogy helps explain its mechanical behavior:

Table 3.1: Typical mineralogical composition of Tournemire shale

Mineral	Content (%)	Impact on Properties
Clay minerals	40-50	Controls plasticity and swelling
Quartz	20-25	Provides stiffness
Calcite	15-20	Affects brittleness
Other minerals	10-15	Minor influence

The high clay content explains why this shale shows:

- Significant anisotropy due to preferred clay particle orientation
- Sensitivity to water content and pore pressure
- Time-dependent behavior under sustained loads

3.1.2 Laboratory Testing and Geomechanical Characterization

Laboratory tests are essential and remain the most reliable method to characterize rock mechanical properties. However, while extractingintact core samples is a significant challenge, accurately defining the real in-situ state of stress up to thousands of meters remains the crucial piece of information that must be retrieved. Through a combination of different test types, we can reconstruct the complete stress-strain behavior needed for engineering analysis; A brief overview of the cited laboratory tests is provided below:

Uniaxial compression test represents the simplest loading condition, where a cylindrical sample is compressed along its axis without lateral confinement. This test provides the unconfined compressive strength (UCS), which serves as a fundamental strength parameter. More importantly for anisotropic rocks like shale, by testing samples at different orientations relative to bedding planes, we can map how strength varies with loading direction. This variation is crucial for understanding potential failure mechanisms around wellbores where stress orientations constantly change.

Triaxial compression tests similar to UCT but lateral confinement is added to better simulate subsurface conditions. Under confining pressure, rocks typically show higher strength and more ductile behavior. By testing at multiple confining pressures, we can determine the cohesion and internal friction angle through Mohr-Coulomb analysis. These parameters control shear failure, which is the dominant failure mode in most wellbore stability problems.

Brazilian tensile test consist of an indirect measure of tensile strength, carried out by loading a disc-shaped sample diametrically. Although rocks rarely fail in pure tension underground, yet tensile strength controls hydraulic fracturing initiation, making it essential for determining the upper bound of safe mud weights. For Tournemire shale, these tests revealed tensile strengths ranging from 3.8 to 4.6 MPa, depending on bedding orientation.

3.1.3 From Laboratory Data to Model Parameters

The transformation of laboratory test results into numerical model parameters represents a critical step in geomechanical modeling; Since laboratory specimens represent a local and limited image of the subsurface due to their small size (centimeters) and issues with integrity, tuning the parameters to fit the reservoir scale requires considerable expert judgment. However, Lab tests provide controlled conditions where individual mechanical properties can be isolated and measured. Typical parameters acquired during this process are Young's modulus E and Poisson's ratio ν from the linear portion of stress-strain curves, or cohesion c' and friction angle ϕ' from Mohr-Coulomb envelope fitting of triaxial tests data. For the specific case of shales, additional complexities arise from their pronounced anisotropy and sensitivity to moisture content, and most often drained and undrained tests are crucial. The bedding-parallel versus bedding-perpendicular properties can differ by factors of 2-3, and the presence of weak interfaces requires special attention.

The specific input values inserted in each model are detailed in the following sections.

3.2 Constitutive Models and Their Implementation

A constitutive model is a mathematical tool that helps to describe the response of a material (i.e. rock formations) to applied loads, by linking together stress and strain responses and relationships under determined loading and boundary conditions. The term "constitutive" stays there to connect the intrinsic mechanical properties of the rocks with loading conditions. Hence, it helps to define why a sandstone behaves differently from a shale, or what distinguishes intact rock from fractured rock. In practical terms, a constitutive model answers the

question: "Given a certain stress state, what deformation will occur, and will the material undergo failure?". In the field of wellbore stability, this translates to predicting whether the rock around a borehole will remain intact, deform elastically, yield plastically, or fracture when subjected to drilling-induced stresses.

3.2.1 Work Flow for Models Introduction

The constitutive models used in this study form a logical progression from simple to complex, each adding capabilities to address specific aspects of shale behavior:

COMPLEX	KITY PROGRESSION OF CONSTITUTIVE MODELS
Pure Elastic Models (ILE, TIE):	Reversible deformation only. ILE: isotropic properties. TIE: elastic anisotropy for bedding-induced stiffness. No failure prediction.
Isotropic Plasticity (ILE-MC):	Adds Mohr-Coulomb yield criterion for irreversible deformation. Simplest failure model, assumes homogeneous rock.
Anisotropic Strength (UBI):	Dual failure mechanisms: intact rock + sliding along bedding planes. Captures preferential failure of layered rocks.
Full Anisotropy (CANISO):	Combines elastic anisotropy with directional strength. Most realistic for shale: captures both stiffness and strength variations.

Figure 3.1: Hierarchy of constitutive models implemented in FLAC2D used in this work

3.2.2 Isotropic Linear Elastic Model (ILE)

The isotropic linear elastic model represents the simplest approach, assuming the rock behaves as a homogeneous, isotropic material following Hooke's law. This constitutive relationship establishes direct proportionality between stress and strain through two independent elastic constants, typically expressed as Young's modulus (E) and Poisson's ratio (ν) , or alternatively as bulk modulus (K) and shear modulus (G). The model assumes that all the material properties are identical in all directions and full strain reversibility, thus no permanent deformation upon unloading. Despite its simplicity, this model provides a valuable baseline for validation against analytical solutions (Lamé and Kirsch) and serves as a reference for evaluating the effects of more complex behavior.

In the FLAC2D implementation of ILE under dry conditions, that is to say pore pressure equals zero, the constitutive behavior is fully defined by specifying the elastic moduli and density. The key parameters implemented in the model code are:

Table 3.2: ILE dry model parameters for dry conditions

```
; Elastic properties
prop density=2500 ; Rock density [kg/m3]
prop bulk=1.029e10 ; Bulk modulus K = 10.29 GPa
prop shear=9.05e9 ; Shear modulus G = 9.05 GPa
```

For undrained conditions, the key difference is the activation of pore pressure effects. Note that in all undrained cases from now on, the pore pressure value will always be set on $11 \ MPa$ and kept as a reference; the same applies for porosity and permeability values in the following simulations.

Table 3.3: ILE undrained model parameters

```
; Fluid properties
prop porosity=0.22 ; Porosity
prop perm=3e-13 ; Permeability
water density=1000 ; Water density [kg/m3]
water bulk=2e9 ; Water bulk modulus Kw = 2 GPa
;;
Initial conditions
ini pp 11e6 ; Initial pore pressure = 11 MPa
```

The pore pressure of 11 *MPa* represents typical conditions at approximately 1100 *m* depth, assuming hydrostatic gradient. The water bulk modulus controls the pore pressure generation under undrained loading conditions according to Skempton's theory already discussed in Section 2.6. When the rock is compressed, both the solid skeleton and the pore water must accommodate the deformation.

3.2.3 Transversely Isotropic Elastic Model (TIE)

The transversely isotropic elastic model extends the elastic structure to capture the natural anisotropy of layered and stratified rocks such as shale; unlike the ILE model, TIE recognizes that elastic properties differ between directions parallel and perpendicular to bedding planes. The TIE model is implemented in the software under the anisotropic model framework, which requires a set of parameters to be implemented in the code as reported in Table 3.4 below.

During deposition and compaction, shale's alike rocks develop a directional dependence due to the preferential alignment of clay platelets during the millennial settling process, creating a material that is better described in geomechanics by five independent elastic constants instead of the two required for isotropy. The model maintains linear elasticity but accounts for the systematic variation of stiffness with loading direction; thus, bedding planes are axes of elastic symmetry. The **transverse isotropy** assumption implies that properties are identical in all directions parallel to bedding (the plane of isotropy) but different in the perpendicular direction. This simplification is well-suited for horizontally bedded shales where vertical and horizontal properties show the most significant contrast, expressed in oil and gas field as a ratio $R = \frac{\sigma_{Hmax}}{\sigma_{hmin}}$, which differs from the K_0 we have seen in 2.1.1.

Table 3.4: TIE model parameters in FLAC2D

```
; Activate anisotropic elastic model
model anisotropic
; Elastic properties
prop density=2500
                       ; Rock density [kg/m3]
prop angle=0
                         Bedding orientation [degrees from horizontal]
prop xm = 21e9
                       ; E parallel to bedding = 21 GPa
                       ; E perpendicular to bedding = 12.5 GPa
prop ym=12.5e9
                       ; Shear modulus G12 = 6.71 GPa
prop shear = 6.71e9
prop nuy = 0.08
                        Poisson's ratio nu12 (in-plane)
prop nuz=0.16
                        Poisson's
                                    ratio nu23 (out-of-plane)
```

The anisotropy ratio of $E_{\parallel}/E_{\perp} \approx 1.7$ is typical for shales and significantly affects stress concentrations around wellbores. The lower stiffness perpendicular to bedding leads to preferential deformation in this direction and modified stress distributions compared to isotropic assumptions.

3.2.4 Mohr-Coulomb Elastoplastic Model (ILE-MC)

The Mohr-Coulomb model instead, goes beyond pure elasticity and introduces plastic yielding when the shear stress state reaches the material's strength limit. This elastoplastic formulation captures the transition from reversible deformation to permanent failure, essential for predicting wellbore breakouts and collapse. The yield surface is defined by the linear Mohr-Coulomb criterion in principal stress space:

$$\sigma_1' = C_0 + N_\phi \sigma_3'$$

where $C_0 = 2c' \cos \phi' / (1 - \sin \phi')$ represents the uniaxial compressive strength and $N_{\phi} = (1 + \sin \phi') / (1 - \sin \phi')$ is the confinement factor.

Table 3.5: Mohr-Coulomb model parameters in FLAC2D

```
model mohr
                      ; Activate Mohr-Coulomb plasticity
; Elastic properties (pre-yield behavior)
prop density=2500
                      ; Rock density [kg/m3]
prop bulk=1.09e10
                      ; Bulk modulus K = 10.9 GPa
prop shear=9.05e9
                      ; Shear modulus G = 9.05 GPa
; Plastic properties (post-yield behavior)
prop cohesion=8.37e6 ; Cohesion c' = 8.37 MPa
                   ; Friction angle phi = 33 degrees
prop friction=33.0
prop dilation=0.0
                      ; Dilation angle psi = 0 degrees
                   ; Tensile cutoff = 3.0 MPa
prop tension=3.0e6
```

The zero dilation angle represents a conservative assumption preventing volumetric expansion during shear. The tensile cutoff, as a rule of thumb, has been taken as one tenth of the computed UCS:

$$C_0 = \frac{2c'\cos\phi'}{1-\sin\phi'} = \frac{2\cdot 8.37MPa \cdot \cos(33)}{1-\sin(33)} = 30.8MPa \Rightarrow T_0 \approx \frac{30}{10}Mpa = 3MPa$$

the introduction of the this value prevents unrealistic tensile stresses from developing.

3.2.5 Ubiquitous Joint Model (UBI)

The Ubiquitous Joint model offers a powerful approach to rock failure analysis by integrating the Mohr-Coulomb criterion with the Weakness Plane model to explicitly address the presence of a preferentially oriented weakness plane embedded within an intact rock matrix. In essence, the rock is not treated as a single uniform material, and this feature is particularly relevant for shales where bedding planes act as systematic planes of weakness while the intact rock follows a simpler criterion. In detail, this model evaluates two potential failure modes at each stress state: (i) intact rock failure following the Mohr-Coulomb criterion, and (ii) sliding along the predefined joint orientation according to the Weakness Plane Model. Failure can occur

in the rock matrix, along the weakness planes, or simultaneously in both. The controlling mechanism is the one that activates at the lower stress level.

Table 3.6: Ubiquitous Joint model parameters

```
model ubiquitous
                         ; Activate ubiquitous joint model
  ; Matrix properties (intact rock)
  prop density=2500
                         ; Rock density [kg/m3]
  prop bulk=1.09e10
                         ; Bulk modulus K = 10.9 GPa
                        ; Shear modulus G = 9.05 GPa
  prop shear=9.05e9
  prop cohesion=8.37e6 ; Matrix cohesion = 8.37 MPa
                        ; Matrix friction = 33 degrees
  prop friction=33.0
  prop tension=3.0e6
                         ; Matrix tension = 3.0 MPa
                         ; Matrix dilation = 0 degrees
  prop dilation=0.0
  ; Joint properties (weakness plane)
  prop jangle=0.0
                         ; Joint orientation [degrees]
  prop jcohesion=4.26e6; Joint cohesion = 4.26 MPa
14
  prop jfriction=32.0
                        ; Joint friction = 32 degrees
  prop jtension=3.8e6 ; Joint tension = 3.8 MPa
                         ; Joint dilation = 0 degrees
  prop jdilation=0.0
```

The joint cohesion at approximately 50% of matrix cohesion reflects the reduced cementation along bedding interfaces, while similar friction angles indicate comparable surface roughness characteristics.

3.2.6 CANISO Model

Following the Ubiquitous Joint model, we introduce the CANISO model, which represents the most comprehensive constitutive formulation. It combines transversely isotropic elasticity with orientation-dependent weakness—plane plasticity. Input parameters are shown in the Table 3.7.

Table 3.7: CANISO model parameters

```
; Activate CANISO model
  model caniso
  ; Anisotropic elastic properties
  prop density=2500
                         ; Rock density [kg/m3]
  prop angle=0
                         ; Material orientation [degrees]
  prop e1=21e9
                         ; E parallel to bedding = 21 GPa
  prop e2=12.5e9
                         ; E perpendicular = 12.5 GPa
  prop g2=6.71e9
                         ; Out-of-plane shear modulus
  prop nu1=0.08
                         ; Poisson's ratio nu12
9
  prop nu2=0.16
                         ; Poisson's ratio nu23
10
11
  ; Joint/weakness plane properties
  prop jcohesion=4.26e6 ; Joint cohesion = 4.26 MPa
  prop jfriction=32.0
                       ; Joint friction = 32 degrees
14
  prop jtension=3.8e6
                         ; Joint tension = 3.8 MPa
  prop jdilation=0.0
                       ; Joint dilation = 0 degrees
```

This model simultaneously captures elastic anisotropy (different stiffnesses in different directions) and strength anisotropy (variation of failure criteria with loading orientation). The elastic response follows the TIE formulation, while the plastic behavior incorporates weakness planes similar to UBI but within a fully anisotropic elastic framework. This advanced model is particularly suited for situations where both pre-failure deformation patterns and ultimate strength depend strongly on bedding orientation, as commonly observed in shale formations.

3.3 Summary and Next Steps

This chapter has presented the geomechanical dataset for Tournemire shale and introduced the constitutive models and their parameters that will be used in the numerical analysis. This has been done to provide a comprehensive framework for understanding shale behavior around wellbores, starting from a simple elastic model (ILE) up to a complex anisotropic model such as CANISO. In the next chapter we will detail the numerical mesh and boundary conditions in the software, and then introduce the first crucial point: validating the numerical setup against Kirsch analytical solutions presented in Section 2.2.2. This validation will ensure that our numerical implementation correctly captures the fundamental elastic behavior before proceeding to more complex analyses involving plasticity and anisotropy.

FLAC2D: Implementation and Validation of Models

4.1 Introduction

This chapter delves into the FLAC2D setup; in particular, we present a first overview of the software and the grid we have used for the analysis. Then the numerical setup will be tested by doing a direct comparison between the results obtained from the first constitutive model (ILE dry) and the analytical plot that must be obtained with Kirsch solution in both sections A and B, as extensively discussed in 2.2.2, this will serve as baseline for the following complex models. In the end, a comparison with TIE in dry conditions is also introduced to spot the main differences that arise when anisotropy is introduced.

4.2 FLAC2D Software Overview

FLAC2D (Fast Lagrangian Analysis of Continua in 2 Dimensions) is a continuum mechanics code that uses an explicit finite difference method to perform its calculation, which differs from other finite element methods since it employs a Lagrangian calculation scheme that is particularly well-suited for problems involving large deformations, material nonlinearity, and complex constitutive behavior. This approach is especially valuable for wellbore stability analysis where the transition from elastic deformation to plastic failure must be accurately captured.

4.2.1 Mesh, Grid and Configuration

The creation of wellbore requires a circular geometry by its nature, so the modeling must necessarily follow this scheme. Although FLAC is based on C++, it allows through built-in functions such as the DONUT function to construct a mesh to represent what happens around the well in a symmetrical and radial manner. This creates an annular mesh that extends from the wellbore radius to the far-field boundary, ensuring optimal element distribution for capturing the steep stress gradients near the excavation.

In FLAC2D, the polar mesh elements are indexed using an (i,j) system where:

- Index i: represents the radial direction (i=1 at inner boundary, i=61 at outer boundary)
- Index j: represents the circumferential direction (j=1 at $\theta = 0^{\circ}$, increasing counter-clockwise up to j=61 coinciding with j=1)

This indexing nomenclature is crucial in order to extract the results at specific locations: Sector A ($\theta = 0^{\circ}$) corresponds to j=1 while Sector B ($\theta = 90^{\circ}$) corresponds to j=16.

The mesh geometry follows a geometric progression to concentrate elements where needed; grid structure made on FLAC is reported in Figure 4.1 and its geometrical parameters are detailed in Table 4.4.

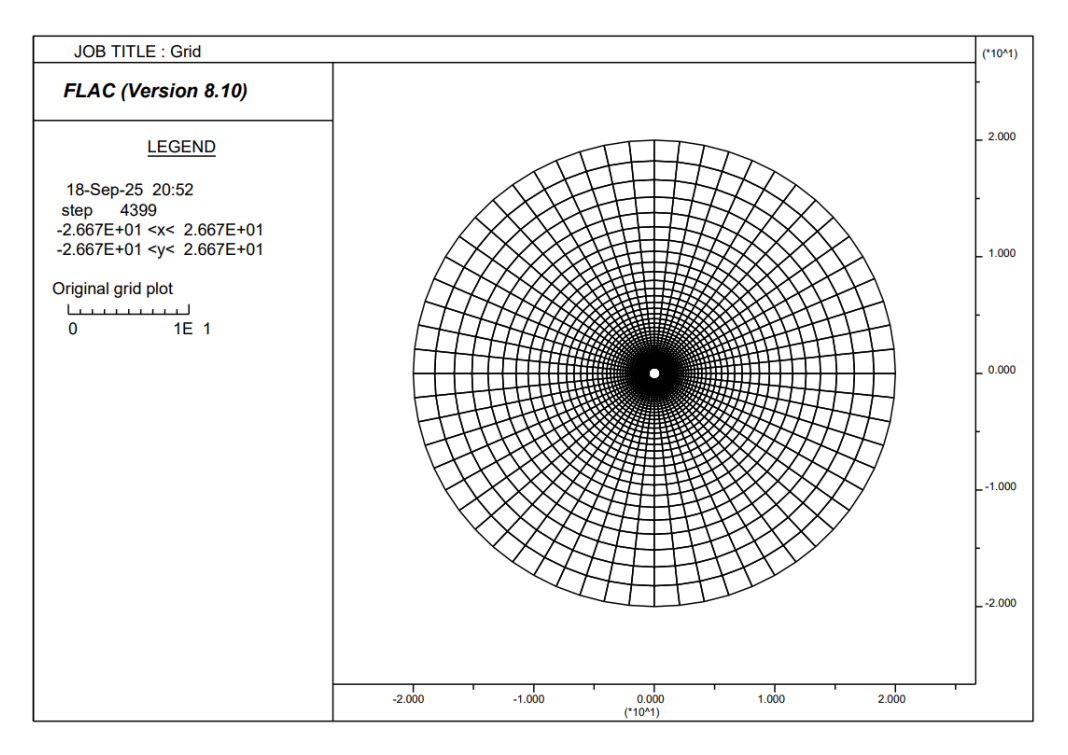


Figure 4.1: polar mesh implemented in FLAC2D showing the grid structure: 60 radial x 60 circumferential zones.

Table 4.1: Mesh parameters for polar grid generation

```
; Mesh geometry parameters
  set rmin=0.5
                    ; Inner radius (wellbore) [m]
  set rmul=40.0
                    ; Radius multiplier Rout/Rmin
  set gratio=1.1
                    ; Geometric grading ratio
                    ; Number of radial zones
  set izone=60
  set jzone=60
                    ; Number of circumferential zones
6
  ; Calculated parameters
  ; Rout = rmin * rmul = 0.5 * 40 = 20 m
  ; Angular increment = 360/60 = 6 degrees per zone
  ; Total elements = 60 * 60 = 3600 quadrilaterals
```

4.3 Boundary Conditions and Initial State of Stress

The mesh geometry of the model represents a vertical wellbore at depth where the in-situ stresses have already been established. The principal horizontal stresses, as illustrated in Fig.4.2 σ_{Hmax} is acting in the x-direction (Sector A) and σ_{hmin} in the y-direction (Sector B). These values represent typical conditions at approximately 1100 m depth in a normal faulting stress regime, and are better known as far-field stresses.

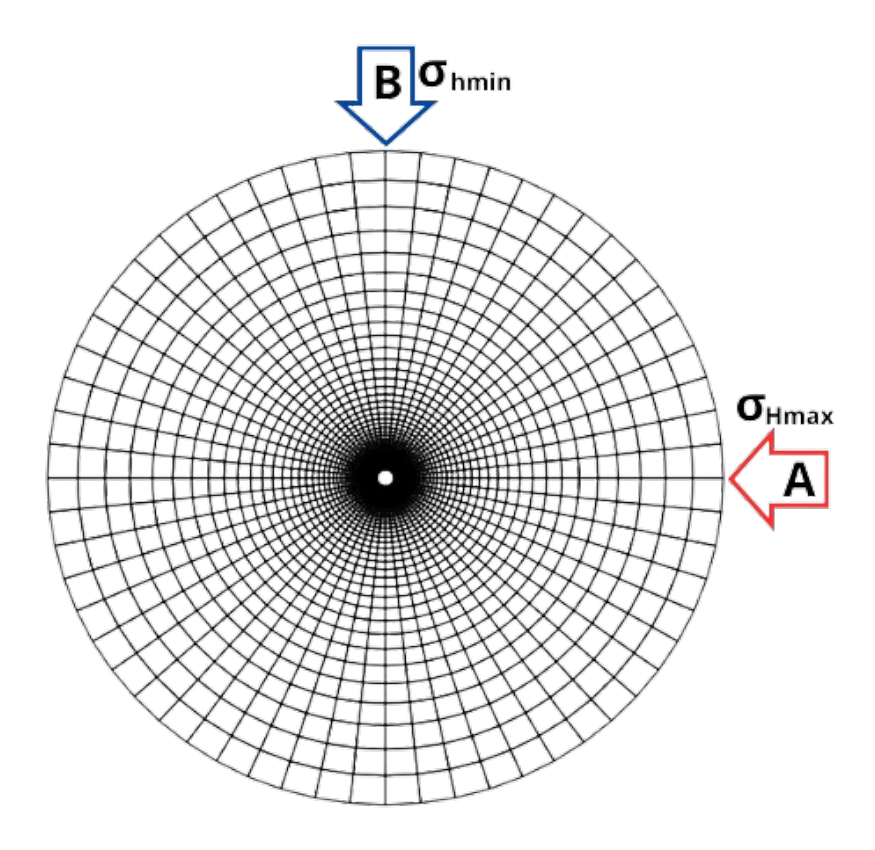


Figure 4.2: Orientation of far-field stresses in the numerical model; $\sigma_{Hmax} = 30 \ MPa$ acts along the x-axis, while $\sigma_{hmin} = 20 \ MPa$ acts along the y-axis. The wellbore axis is perpendicular to the page.

The selected stress magnitudes represent a case in which $\sigma_{Hmax} > \sigma_v > \sigma_{hmin}$, thus the resulting anisotropy ratio is $R = \frac{\sigma_{Hmax}}{\sigma_{hmin}} = 1.5$. These conditions are typical for many sedimentary basins and provide a comparative case to field application. The Table 4.2 shows how these specific parameters have been implemented as boundary conditions of the mesh.

Table 4.2: Boundary conditions and initial stress state

```
; Initial stress state (compression negative in FLAC2D)
ini sxx -30e6 ; Sigma Hmax = 30 MPa (E-W direction)
ini syy -20e6 ; Sigma hmin = 20 MPa (N-S direction)
ini szz -25e6 ; Sigma v = 25 MPa (vertical/out-of-plane)

; Boundary conditions at outer radius (i=61)
apply sxx -30e6 from 61,1 to 61,61
apply syy -20e6 from 61,1 to 61,61

; Wellbore pressure at inner radius (i=1)
apply pressure 0e6 from 1,1 to 1,61 ; Open hole condition
```

Even if in this case the wellbore pressure, thus the mud pressure, has been set to 0, it will vary in our analysis to better capture the differences among the models, especially under drained and undrained conditions.

4.4 Validation: ILE vs. Kirsch

In order to make sure that all the previous mesh and boundary conditions were well-structured and properly done, the first step was to compare FLAC2D results for the *isotropic linear elastic*, under dry conditions case against the analytical Kirsch solution at the borehole wall and away from the hole.

Setup ILE $\sigma_{H \text{ max}} = 30MPa$, $\sigma_{h \text{ min}} = 20MPa$, $\sigma_v = 25MPa$, and $p_w = 0MPa$. Under dry conditions $(p_w=0)$ where total and effective stresses coincide.

4.4.1 Kirsch Results

Borehole wall: At the borehole wall $(r = R_w)$ the radial stress equals mud pressure, $\sigma_r(R_w) = p_w$ while the hoop stress along the two principal azimuths is:

A:
$$\theta = 0^{\circ} \implies \sigma_{\theta}(R_w) = 3 \sigma_{h \min} - \sigma_{H \max} - p_w = 3 \cdot 20 - 30 - 0 = 30 MPa,$$
 (4.1)

B:
$$\theta = 90^{\circ} \implies \sigma_{\theta}(R_w) = 3 \sigma_{H \max} - \sigma_{h \min} - p_w = 3 \cdot 30 - 20 - 0 = 70 MPa.$$
 (4.2)

Therefore, σ_{θ} at the wall is 30MPa in A and 70MPa in B, while $\sigma_r(R_w) = p_w = 0MPa$.

Farfield stresses: Moving away from the hole, the numerical curves converge to the farfield values in the corresponding directions, as predicted by Kirsch:

Hoop stresses

$$\sigma_{\theta}(r \to \infty, \theta = 0^{\circ}) = \sigma_{h \min} = 20MPa,$$
 (4.3)

$$\sigma_{\theta}(r \to \infty, \theta = 90^{\circ}) = \sigma_{H \,\text{max}} = 30.MPa$$
 (4.4)

Radial stresses

$$\sigma_r(r \to \infty, \theta = 0^\circ) = \sigma_{h \min} = 20MPa,$$
 (4.5)

$$\sigma_r(r \to \infty, \theta = 90^\circ) = \sigma_{H \,\text{max}} = 30 MPa.$$
 (4.6)

Close to the borehole wall, σ_{θ} is the major principal stress, on the other hand σ_{r} equals the mud pressure; with increasing r a *principal-stress swap* occurs and the stress components align with the far-field tensor. This inversion is visible in the FLAC2D curves.

4.4.2 FLAC2D Results Comparison

Outcome. The results outcome from numerical calculations are illustrated in Figures 4.3–4.4 in which $\sigma_{\theta}(r)$ and $\sigma_{r}(r)$ from FLAC2D are plotted along sectors A ($\theta = 0^{\circ}$) and B ($\theta = 90^{\circ}$) against r. At the wall, the numerical values match the analytical targets:

- Sector A: $\sigma_{\theta}(R_w) \approx 30MPa$, $\sigma_r(R_w) = 0MPa$.
- Sector B: $\sigma_{\theta}(R_w) \approx 70MPa$, $\sigma_r(R_w) = 0MPa$.

These outcomes confirm the reliability of our model in terms of: (i) mesh density and grading (that capture the near-wall gradients apart from spurious anomalies explained in Section 4.6); (ii) boundary conditions reproduce the intended far-field state of stress; (iii) stress calculations along both sectors A/B is consistent.

This provides a solid baseline to proceed with anisotropy (TIE) and plasticity (ILE–MC, UBI, CANISO), whose direct analytical validation is not easily feasible.

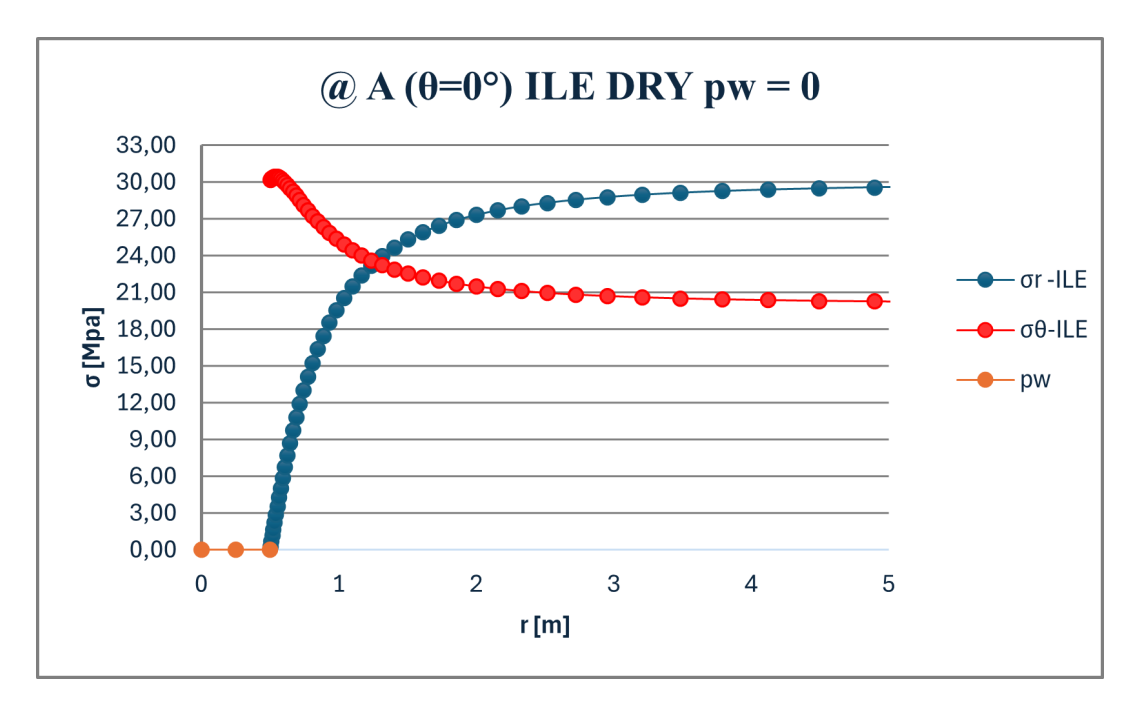


Figure 4.3: Sector A ($\theta=0^{\circ}$): FLAC2D vs. Kirsch trends for hoop and radial stresses.

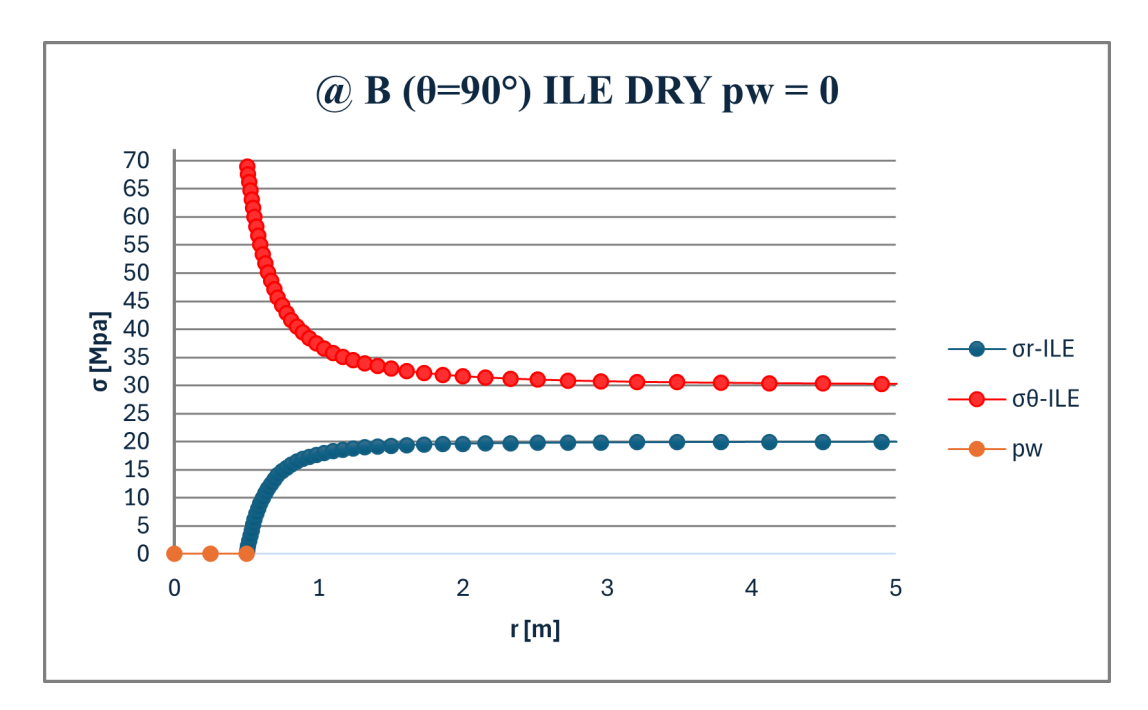


Figure 4.4: Sector B (θ =90°): FLAC2D vs. Kirsch trends for hoop and radial stresses.

4.4.3 ILE vs. TIE (dry conditions)

A straight comparison between the isotropic linear elastic model and the transversely isotropic elastic model is proposed in this section, to highlight and spot any possible discrepancies among them as anisotropy is introduced.

In detail, Figure 4.5–4.6 shows the radial profile of σ'_r and σ'_θ in A $(\theta = 0^\circ)$ and B $(\theta = 90^\circ)$ for both ILE and TIE, to better visualize the small changes.

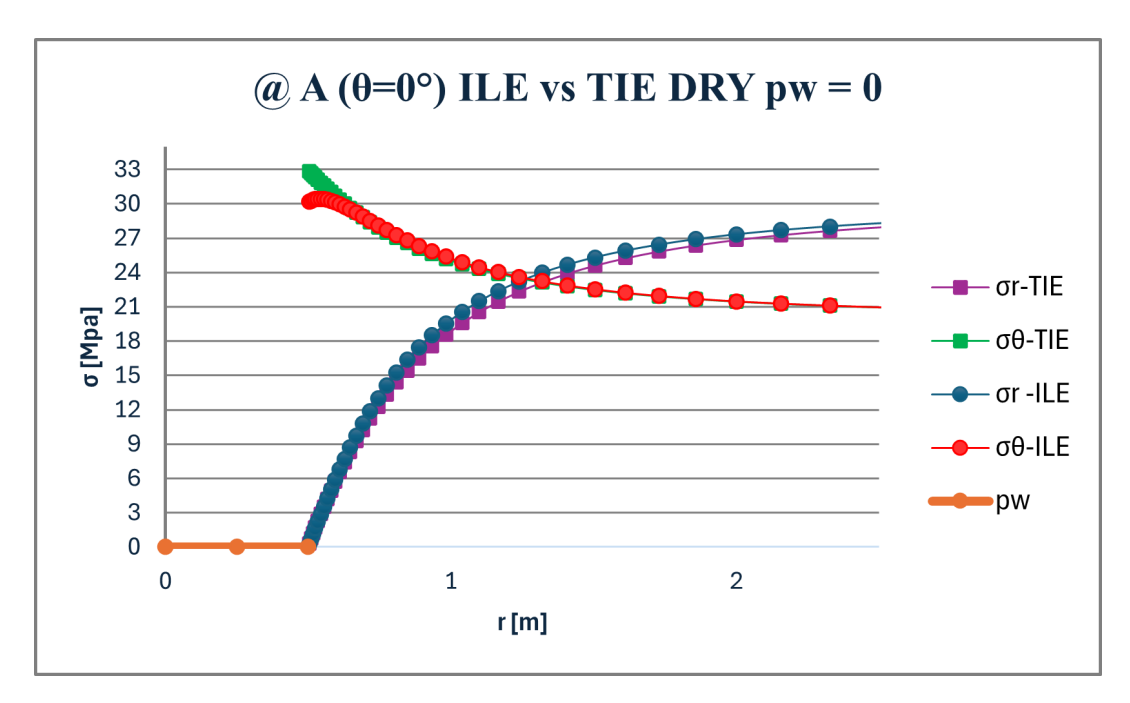


Figure 4.5: Radial profile of σ_r and σ_θ in A $(\theta = 0^\circ)$: ILE vs TIE, dry, $p_w = 0$.

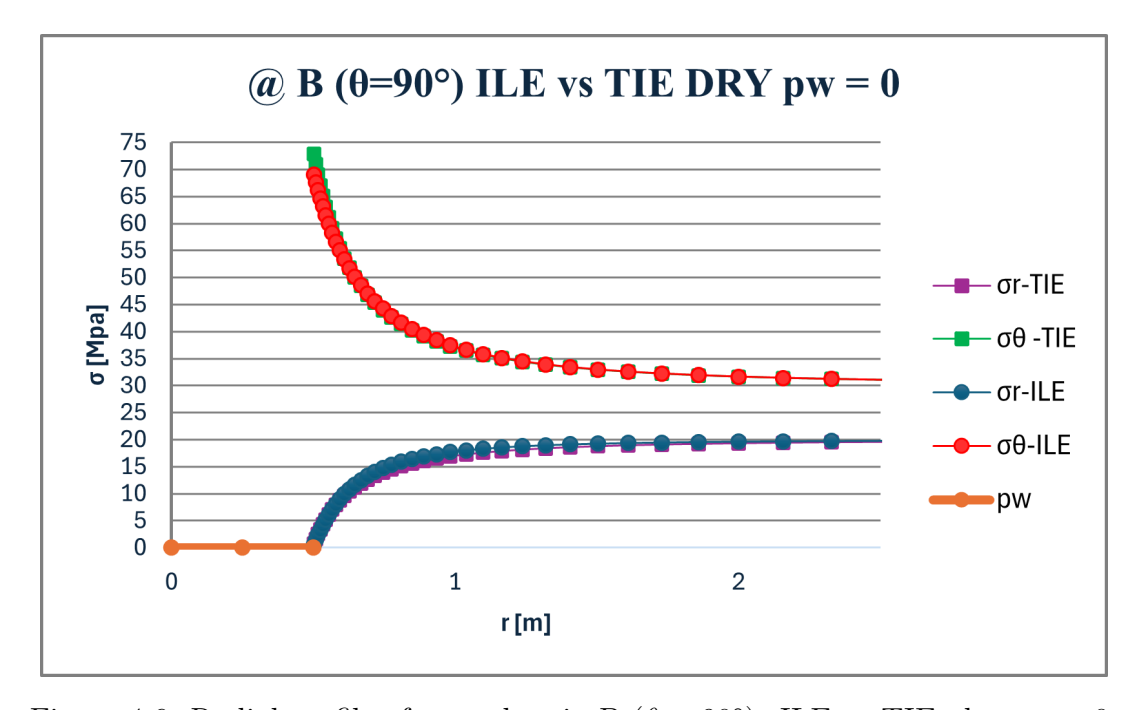


Figure 4.6: Radial profile of σ_r and σ_θ in B ($\theta = 90^\circ$): ILE vs TIE, dry, $p_w = 0$.

As we can appreciate from the plots, TIE model predicts slightly higher σ_{θ} (few MPa) in both A and B sections, suggesting a higher concentration of hoop stresses in an anisotropic material. This result is consistent with moderate anisotropy such as that of Tournemire shale. A lower stiffness along a specific direction allows for higher local displacements; thus, in order to satisfy the local equilibrium near the wellbore zone, the σ_{θ} amplifies, especially in the most critical section such as B. The σ_r instead, is still constrained to the mud pressure value (0 in this case) at the borehole wall (inner radius), which is its starting point. However, the radial gradient with which it rises is directly dependent on the stiffness tensor, which explains the slight difference in the radial profile. Overall, both ILE and TIE reach the same far-field stress values, demonstrating how, despite the local differences, the consistency of our model is trustworthy. In general, the anisotropy governs these discrepancies, even if it's elastic; the different the Poisson's ratio or anisotropy ratio, the higher the odds.

4.5 MWW Calculation

Here the Mud Weight Window (MWW) calculations are reported following (i) what has already been seen in Section 2.4 - using Eqs. 2.17-2.20 and then moving to (ii) Weak Plane Model (WPM, Jaeger) failure condition, which considers the slip on weak planes. The latter case has been computed in Excel and the results are published.

4.5.1 Matrix-controlled Window (Mohr-Coulomb)

Data (Tournemire). $\sigma_H = 30$ MPa, $\sigma_h = 20$ MPa, $p_f = 11$ MPa. Matrix parameters: c' = 8.37 MPa, $\varphi' = 33^{\circ}$, $C_0 = 30.8$ MPa, $T_0 \simeq 3$ MPa and $T_0 \simeq 3$ MPa and $T_0 \simeq 3$ MPa. $T_0 \simeq 3$ MPa.

Sector B - Lower bound - Shear Failure: Here the highest value of $p_{w,min}$ was obtained for the case of: $\sigma_{\theta} > \sigma_z > \sigma_r$, the computations are referred to the borehole wall:

$$\sigma'_{\theta}(B) = 3\sigma'_H - \sigma'_h - p'_w, \qquad \sigma'_r(B) = p'_w.$$

Failure when $\sigma_1' = N_\phi \, \sigma_3' + C_0$ with $(\sigma_1', \sigma_3') = (\sigma_\theta', \sigma_r')$ and $p_f = 11MPa$:

$$3\sigma'_H - \sigma'_h - p'_w = N_\phi p'_w + C_0 \implies p'_w = \frac{3\sigma'_H - \sigma'_h - C_0}{N_\phi + 1} = \frac{3 \cdot 19 - 9 - 30.8}{3.397 + 1} \approx 3.92 \text{ MPa.}$$

Totals: $p_{w,\min} = p'_w + p_f \approx 3.92 + 11 = \boxed{14.92 \text{ MPa}}$.

Sector A - Upper bound - Tensile Failure: Calculations are performed at $r = R_W$:

$$\sigma'_{\theta}(A) = 3\sigma'_h - \sigma'_H - p'_w.$$

Tension onset $\sigma'_{\theta}(a, A) = -T_0$ gives

$$p'_{w} = 3\sigma'_{h} - \sigma'_{H} + T_{0} = 3 \cdot 9 - 19 + 3 = 11 \text{ MPa} \Rightarrow p^{\text{frac,matrix}}_{w,\text{max}} = p'_{w} + p_{f} = \boxed{22 \text{ MPa}}$$

Therefore, the range is:

$$MWW_{matrix} = [14.92; 22] MPa.$$

4.5.2 Weak-plane-controlled (WPM, Jaeger)

Jaeger slip criterion on a plane. When shear failure occurs as slip on weak planes and the local ordering is $\sigma_{\theta} > \sigma_z > \sigma_r$, Jaeger's expression for the slip strength is

$$(\sigma_1 - \sigma_3)_{\text{slip}} = \frac{2(c'_w + \sigma'_3 \tan \varphi'_w)}{\left(1 - \frac{\tan \varphi'_w}{\tan \beta_w}\right) \sin 2\beta_w}.$$

Solving at the wall for the mud pressure that brings the weak plane to failure yields the operative form

$$p_w^{\text{slip}}(\theta) = \frac{S\left(1 - \frac{\tan \varphi_w'}{\tan \beta_w}\right) \sin 2\beta_w - 2c_w + 2\tan \varphi_w' p_f}{2\left[\tan \varphi_w' + \left(1 - \frac{\tan \varphi_w'}{\tan \beta_w}\right) \sin 2\beta_w\right]}, S(\theta) = \sigma_{\text{max}} + \sigma_{\text{min}} - 2(\sigma_{\text{max}} - \sigma_{\text{min}}) \cos 2\theta.$$

Here θ is the azimuth around the borehole from the σ_H direction, β_w is the angle between the weak plane and the borehole axis, and for the present vertical well with $\sigma_H > \sigma_h$ we set $\sigma_{\text{max}} = \sigma_H$, $\sigma_{\text{min}} = \sigma_h$. The bedding orientation enters as $\beta_w = \theta - \delta$ (with δ the bedding tilt w.r.t. the principal stresses). The *operative* lower bound is the most restrictive value over the valid azimuth range:

$$p_{w,\min}^{\text{WPM}} = \min_{\theta \text{ (valid)}} p_w^{\text{slip}}(\theta).$$

Parameters (weak planes). $c_w = 4.26$ MPa, $\varphi'_w = 32^\circ$, $p_f = 11$ MPa. Two bedding orientations are considered: $\delta = 15^\circ$ and $\delta = 0^\circ$. Below we show the numerical substitution at the critical azimuths that control the bound.

Case $\delta = 15^{\circ}$ (critical $\theta \approx 80^{\circ}$).

$$\Rightarrow p_w^{\text{slip}}(80^\circ) \approx 18.23 \text{ MPa}$$

This value coincide with the maximum admissible mud pressure, without slip near the critical azimuth; the operative lower bound here is the maximum among all the θ value.

Case $\delta = 0^{\circ}$ (critical $\theta \approx 70^{\circ}$).

$$\Rightarrow p_w^{\text{slip}}(70^\circ) \approx 16.84 \text{ MPa}$$

WPM lower bounds. Thus,

$$p_{w,\min}^{\text{WPM}}(\delta = 15^{\circ}) \approx 18.22 \text{ MPa}, \qquad p_{w,\min}^{\text{WPM}}(\delta = 0^{\circ}) \approx 16.85 \text{ MPa}.$$

The critical azimuth is just the orientation that gives us the tightest limit (or "worst-case scenario") within the acceptable range of stress conditions.

4.6 Sector B - Anomalous Tensile Zones

Carrying out some p_w variations within the same numerical framework, it has been noticed that at the borehole wall in sector B moving around $p_w=p_f=11$ MPa range, local tensile zones appeared. This phenomenon results inconsistent with the elastic reference of the model, since sector B undergoes compression and shear failure is expected to occur. Thus, in this section, we try to determine whether the observed "anomaly" is due to a numerical or physical reason to strengthen the validation process.

TENSION	
COMPRESSION	

Table 4.3: Tension/Compression Maps Legend

Table 4.3 shows the legend for the following pictures, in which (nearly visible) tensile zones are distinguished by a red color.

In particular, the tension region maps showing this occurrence are reported in Fig. 4.7 under undrained conditions for models: MC. UBI and CANISO. Here, the setup to obtain these results is a balanced drilling with $p_w = p_f = 11$ MPa. This phenomenon was observed

37

spuriously even in ILE undrained with overbalance, as we will see in the next chapter; but apart from this anomalous behavior it hasn't been a problem in terms of consistency of the results.

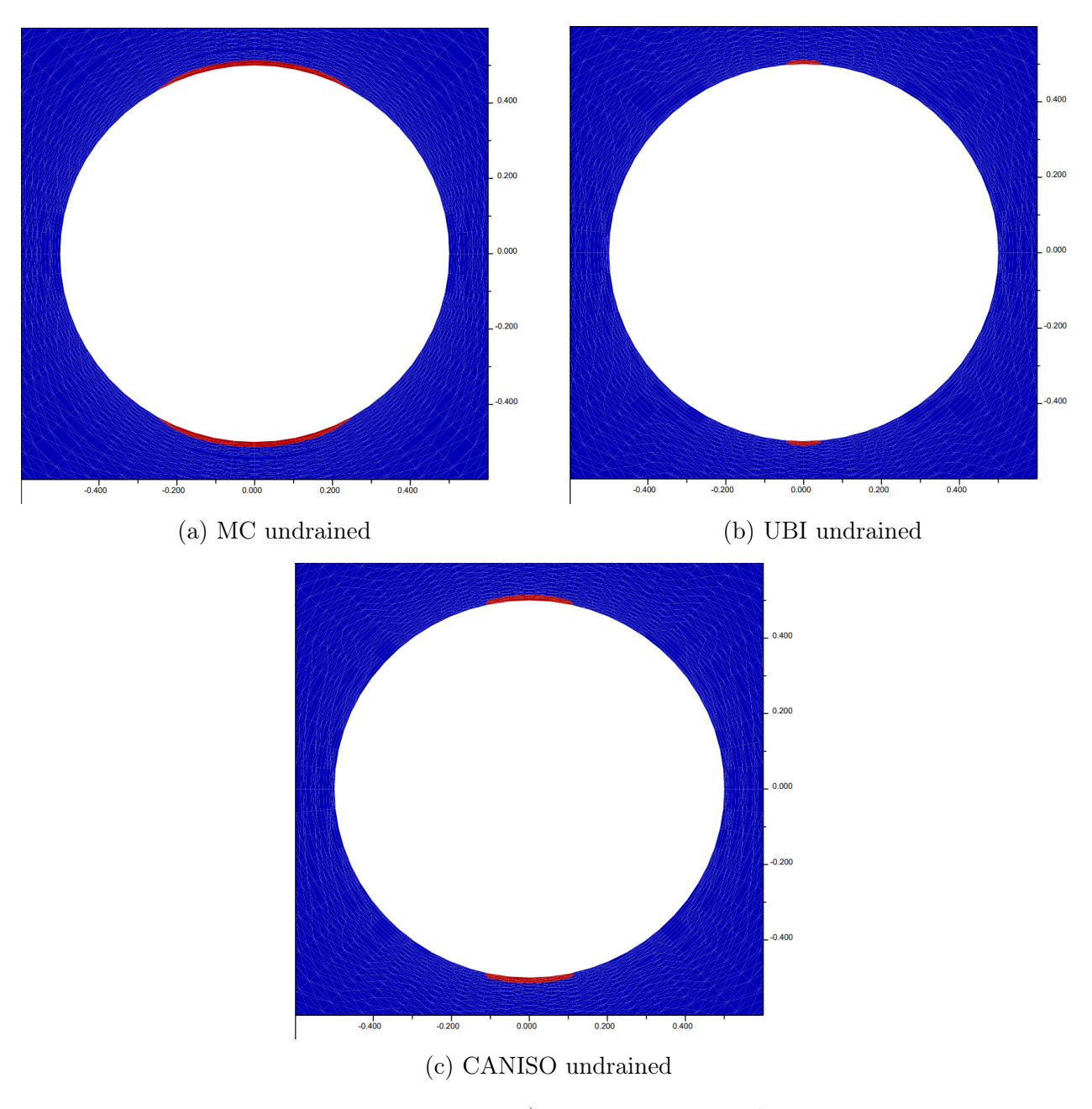


Figure 4.7: Tension/compression anomalies.

What we expected physically and how we dealt with it At the wall in B the total hoop stress σ_{θ} is the largest (compressive) and also the radial one is compressive; thus, the tension should not occur there.

Mesh grading and finer meshes anomaly. The gratio is a geometric parameter that controls the radial growth of grid ring thickness with radius. In general, the *Larger* the gratio the *thinner* (finer) is the first ring at the borehole wall. In our sensitivity tests, increasing gratio (finer at the wall) makes the tiny red zones more visible, while decreasing gratio tends to reduce them.

This behaviour can be attributed to **visualization/discretization artifact** rather than a genuine tensile state. Its origin is unknown and needs a broader investigation, since it

could depend on several model-settings such as discretization, averaging, numerical calculations, post-processing/contouring, and so on. This analysis goes beyond the scope of this thesis work. Practically, we mitigated the issue by reducing \mathtt{gratio} until the tensile pixels disappeared and sector B remained fully compressive.

Mini sensitivity to gratio. With finer grading, as reported in Table 4.5, the wall remains fully compressive in all models. A further examination may be required to verify the effectiveness of this finding and confirm the evidence of the study.

Table 4.4: Mesh parameters for polar grid generation

```
; Mesh geometry parameters
set gratio = 1.10 ; radial grading ratio (roughens near the borehole wall if large)
```

Table 4.5: gratio tuning

Model	gratio		
MC	$1.10 \rightarrow 1.05$		
UBI	$1.10 \rightarrow 1.005$		
CANISO	$1.10 \rightarrow 1.03$		

4.7 Note: FLAC2D - Models Hierarchies

UBI algorithm In FLAC2D, UBI uses a hierarchical sequence: it first evaluates and, if needed, corrects plastic yielding in the *matrix* (Mohr–Coulomb). The updated stresses are then re–evaluated on the predefined weakness plane, where a dedicated slip criterion is checked. In practice, plasticity in the matrix can redistribute stresses and thus either promote or delay subsequent activation of slip along bedding. This order of checks matters when comparing UBI with other models.

CANISO algorithm CANISO instead, is a more direct method. Hence, it doesn't adjust the stress in the surrounding matrix before checking the weak planes; indeed, it checks for slip along the weakness plane immediately on the current stress state and also considers a TIE matrix. This difference between UBI and CANISO is the fulcrum that drives a divergent prediction among the two models: where UBI could point out a matrix yield, CANISO might predict a slip along weakness planes. None of these two predictions is favorable, but having them as a whole can give a broader understanding about failure patterns.

Results and Discussions

In this chapter, we analyze the results of the numerical models and we compare the outcomes of the different constitutive laws: (ILE), Mohr–Coulomb (MC), Ubiquitous Joint (UBI) and CANISO under the same undrained setting ($p_f = 11$ MPa, slight overbalance $p_w > p_f$). For each model we examine wall stress profiles, state maps and (when informative) pore–pressure fields, tracking where and how yielding initiates (matrix shear vs. slip on planes). For UBI and CANISO we also assess the effect of a small bedding tilt ($\delta = 15^{\circ}$). The chapter closes with a concise cross–model recap, highlighting common trends and the distinctive contributions of plastic criteria, weakness planes and elastic anisotropy. Stresses tilt and drained vs undrained in UBI and CANISO models.

5.1 Synthetic Cases - Undrained Conditions

In this section we design a set of synthetic undrained scenarios, in order to compare near well-bore plasticity across various constitutive models under the same framework. Specifically, based on the calculations presented in Section 4.5, we choose a mud pressure value slightly higher than the pore pressure $p_f = 11 \,\mathrm{MPa}$, to activate local yielding without immediately undergoing severe tensile stress or failure; reporting any possible differences among the models. This will permit us to isolate the role of the constitutive model with respect to yielding prediction. Lastly, we will plot the pore pressure behavior among all the constitutive models to better refine and debate the displayed results.

Inputs In table 5.1 are summarized the main inputs common to all undrained runs presented in this section; model-specific parameters were shown in Chapter 3.

Table 5.1: Synthetic case inputs.

Item	Value
Max. horizontal stress $\sigma_{H,max}$	30 MPa
Min. horizontal stress $\sigma_{h,min}$	20 MPa
Stress ratio $R = \sigma_{H \max} / \sigma_{h \min}$	1.5
Pore pressure p_f	11 MPa
Mud pressure p_w	14 MPa $(p_f + \Delta - \text{overbalanced})$
Well radius R_w	as in Chapter 4
Drainage	Undrained conditions
Bedding tilt δ	0° and 15° (when noted)
Principal swap δ^*	swap $\sigma_{H \max} \leftrightarrow \sigma_{h \min}$ (when noted)

For each model we report: (i) wall stress paths $\sigma_{\theta}(\theta)$, $\sigma_{r}(\theta)$; (ii) excess pore-pressure maps

 Δp_f and A/B radial profiles; (iii) plasticity/tension maps and the controlling mechanism at the wall.

5.1.1 Isotropic Linear Elastic (ILE), undrained

The baseline for our study is the first elastic criterion (ILE) under undrained conditions; here, no plasticity is observed due to the elastic behavior of the rock matrix, considered as a whole. The curves here below show *total* hoop and radial stresses (used to validate boundary conditions and Kirsch trends) as done in Section 4.4.2.

Validation The numerical solution follows what we expected from the analytical one: (i) at the wall $\sigma_r = p_w = 14$ MPa in both A and B; (ii) $\sigma_\theta = 3\sigma_{h\,\text{min}} - \sigma_{H\,\text{max}} - p_w = 16$ MPa in A and $\sigma_\theta = 3\sigma_{H\,\text{max}} - \sigma_{h\,\text{min}} - p_w = 56$ MPa in B; (iii) far from the hole, the hoop profiles converge to $\sigma_{h\,\text{min}}$ (A) and $\sigma_{H\,\text{max}}$ (B) and vice versa for σ_r . These checks confirm mesh and boundary conditions and provide the elastic reference for later comparisons.

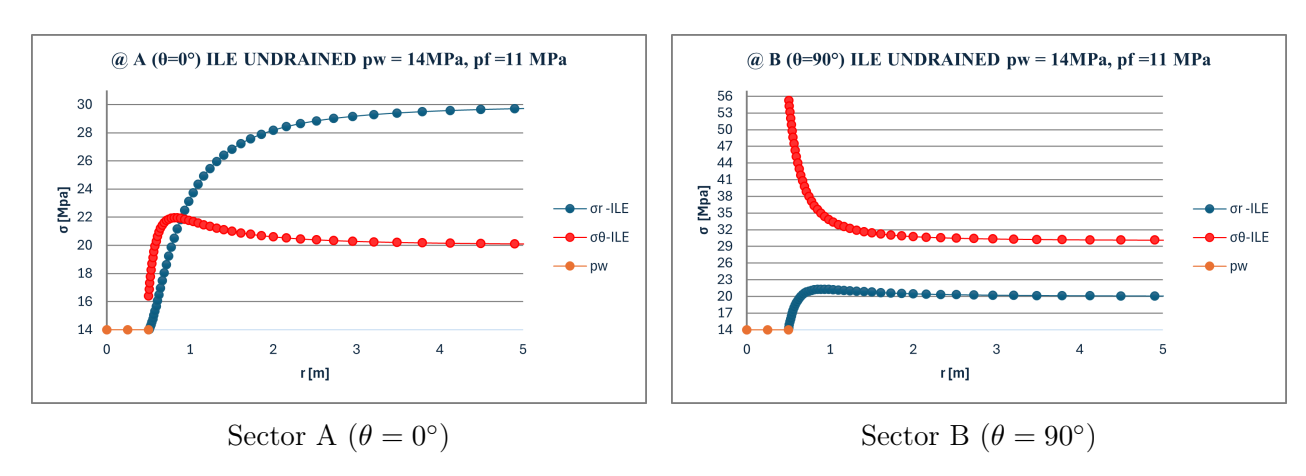


Figure 5.1: ILE undrained, radial profiles of total stresses σ_{θ} (red) and σ_{r} (blue).

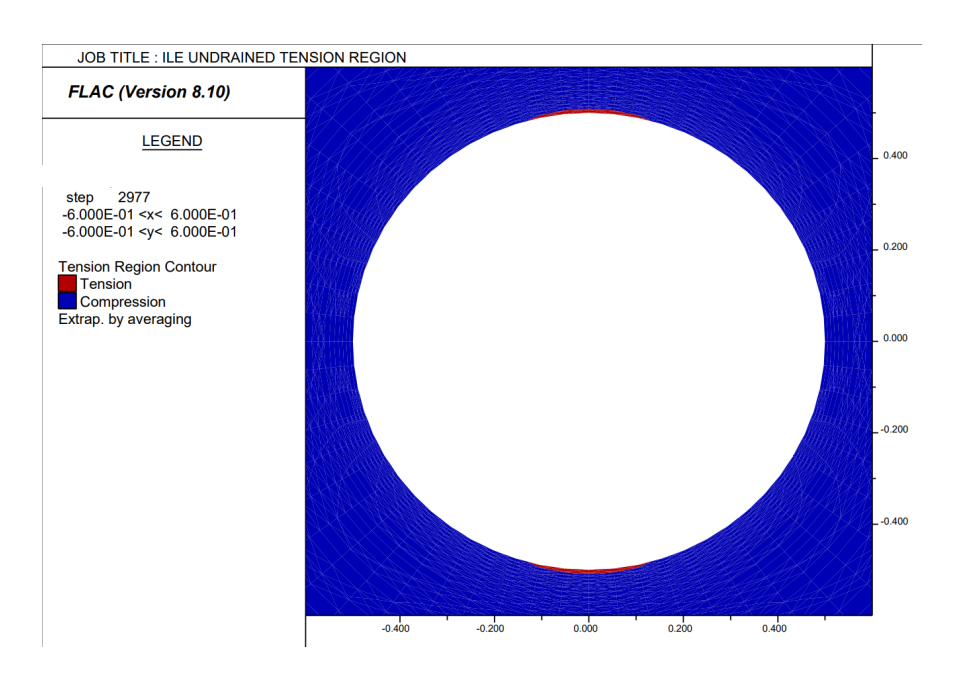


Figure 5.2: ILE undrained tension/compression map.

Discussion (ILE, undrained) Results The undrained elastic run provides a clean baseline to validate both boundary conditions and stress redistribution. The tension/compression

map in Fig. 5.2 highlights two very thin tensile lobes aligned with sector B along the borehole wall; this occurrence was discussed in Section 4.6. Since the material model is purely elastic, no plasticity is activated; indeed, the state map exhibits fully elastic behavior (since it adds nothing new, it has been omitted). Thus, the ILE case simply identifies the azimuths where elasto-plastic models may first reach a tensile cutoff or a lower effective confinement, making the baseline for our investigations.

5.1.2 Mohr-Coulomb (ILE-MC), undrained

Now we are moving to the Mohr-Coulomb constitutive law, keeping the same settings as the previous one; Elastic moduli and strength parameters are those presented in chapter 3.

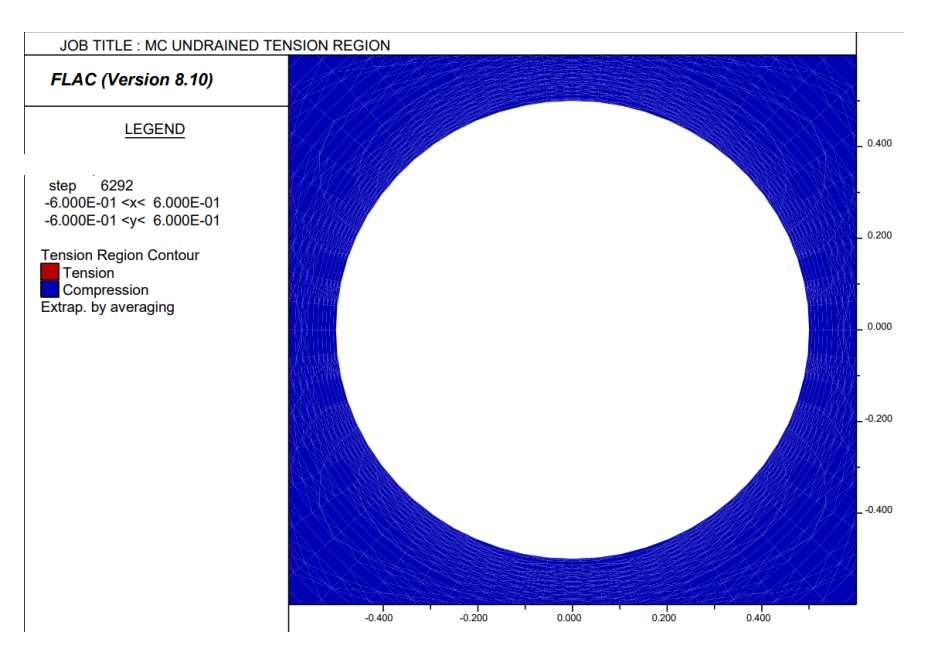


Figure 5.3: MC undrained - tension/compression map.

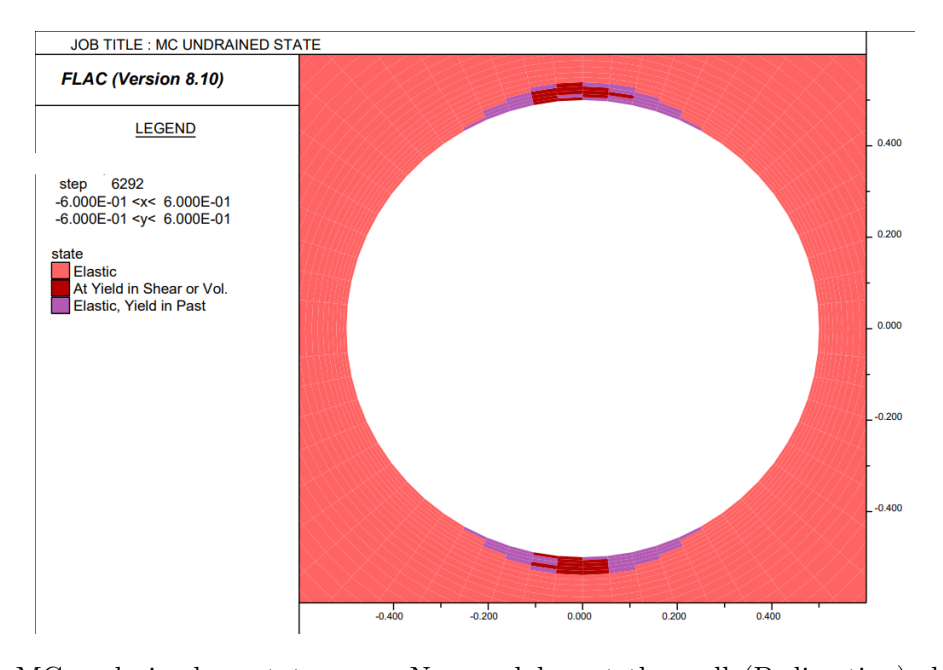


Figure 5.4: MC undrained — state map. Narrow lobes at the wall (B direction) show At Yield in Shear or Vol. and Elastic, Yield in Past. The latter means that yielding occurred during the numerical convergence and the zone is elastic at the end of the step.

Discussion. In slight overbalance $p_w = 14$ MPa above p_f and slightly below the analytical lower bound $p_{w,\min} \approx 14.9$ MPa for the matrix (found with mc criterion in mww and computed in Section 4.5). The tension map is fully compressive whereas the state map shows narrow zones of At Yield in Shear and Elastic, Yield in Past lobes at the wall along sector B. This is consistent with the expected onset of matrix breakout under insufficient mud pressure: plastic shear initiates near the wall where the hoop stress is maximum and the effective confinement is lowest, which is to say in sector B. In the MC model, the matrix is elastic; therefore, "Elastic, Yield in Past" cells indicate zones of transitory activation of yielding during convergence. Even though the yield surface was hit during the iterative solution, the unloading occurred in the elastic domain and at the end of the step the plasticity was recovered (final equilibrium). Whereas, "At Yield in Shear" indicates an unrecoverable yield in the rock matrix that is to say unrecoverable damage. The azimuthal position of the yielded lobes matches the theoretical framework of wellbore stability; MC law shows that the azimuth position of B becomes the first to activate shear (most solicited).

Takeaway The MC constitutive model only represents the intact rock matrix behavior, without including possible effects on the weakness planes or bedding. Hence, any observed plasticity is matrix-controlled, which does not entirely capture the real Tournemire shale pattern of failure, mainly controlled by weakness-plane slip. In the following cases (UBI, CANISO) we will explicitly add weakness planes and anisotropy to assess how slip and strength anisotropy modify both the onset and the spatial extent of failure.

5.1.3 Ubiquitous Joint (UBI), undrained $\delta = 0^{\circ}$

We are now analyzing the Ubiquitous-joint model, which incorporates oriented weakness planes (frictional joint embedded in an elastic-plastic matrix), keeping $p_f = 11 \,\mathrm{MPa}$ and $p_w = 14 \,\mathrm{MPa}$ as in the baseline run. Moreover, since the angle of inclination now matters, we will first examine the $(\delta = 0^\circ)$ scenario (and its results w.r.t. the previous models) and then we will move on to $(\delta = 15^\circ)$ for a comparison.

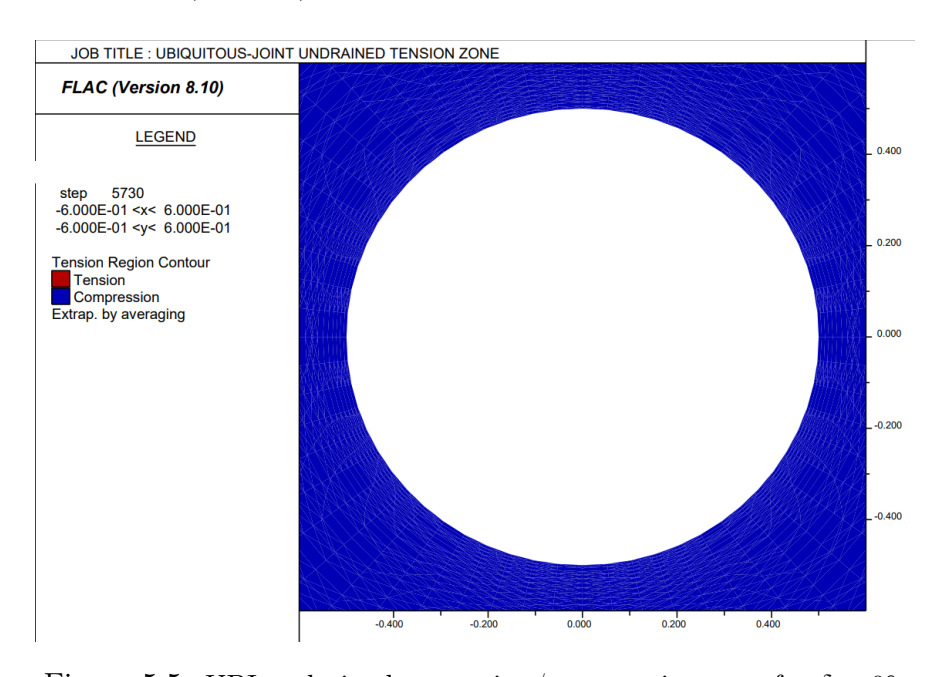


Figure 5.5: UBI undrained — tension/compression map for $\delta = 0^{\circ}$.

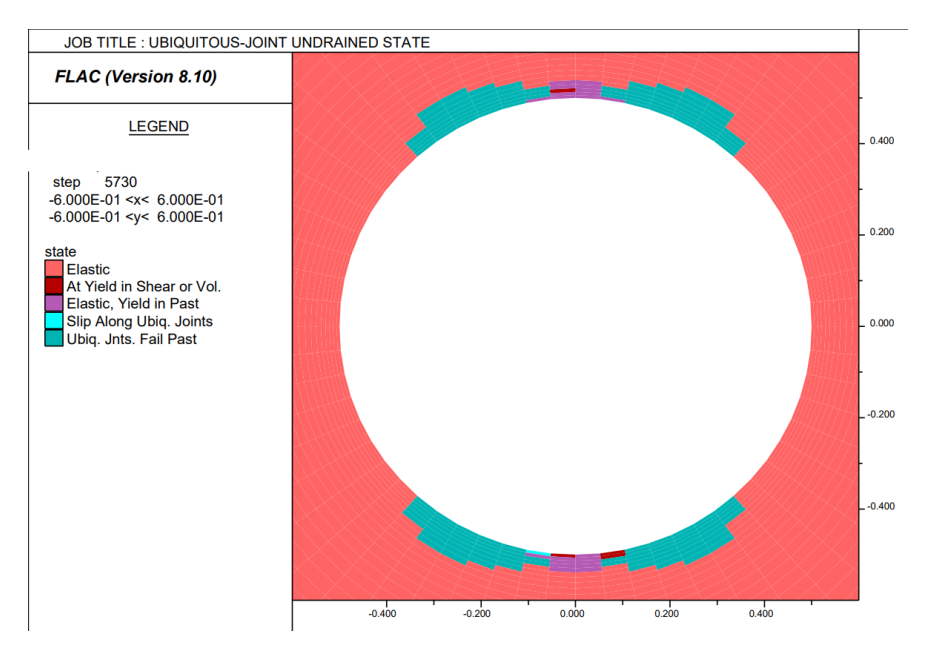


Figure 5.6: UBI undrained — state map for $\delta = 0^{\circ}$.

Discussion. The tension/compression map in Fig. 5.5 remains fully compressive at the wall, corroborating the MC prediction. As in the previous cases $(p_w > p_f)$, but p_w is kept outside the matrix MWW lower bound and well below the weakness-plane capacity. Yet, the state plot exhibits narrow slip lobes centered near sector B (as shown in Fig. 5.6), with only limited matrix yielding at the wall. This is pretty consistent with the (UBI) law and in general with the shale physics: the joint plane, having lower shear resistance than the matrix, mobilizes first (highlighted by *Slip along ubiquitous joints* and *Ubiq. jnts. Fail Past* zones). The areal extent of these slip/past-slip zones is larger than that of matrix-related shear, indicating that weakness planes redistribute stresses over a broader region along their orientation. Matrix yielding remains present but secondary in this scenario.

Key takeaways. Unlike the MC constitutive model, Ubiquitous-Joint activates slip on weakness planes as the first mechanism of yielding. Since joints have a lower shear resistance, the failure along them is not only more visible but also laterally extended, redistributing stresses along bedding and leaving the matrix mostly elastic. As we can appreciate from the state map the yielded matrix is confined just to a small portion.

5.1.4 Ubiquitous Joint (UBI), undrained $\delta = 15^{\circ}$

Since weakness planes have been already introduced, our analysis can be focalized on a slight tilt of the joint system (modulating jangle shown in Section 3.2.5). The physical idea is pretty simple; when a plane isn't aligned with the principal stresses (slanted), the near-wellbore stress field breaks down on that plane into a normal component and a shear component. With a small inclination δ , part of the contrast between σ_{θ} and σ_{r} translates into shear along the plane, while the effective normal stress decreases on the "favored" side. In order to get a clear overview of this relationship, we simply break it down here:

$$\sigma'_n \approx \sigma_r \cos^2 \delta + \sigma_\theta \sin^2 \delta - p_f, \qquad \tau_j \approx \frac{1}{2} (\sigma_\theta - \sigma_r) \sin 2\delta,$$

so that for $\delta > 0$ the available τ_j increases and σ'_n locally decreases. Since slip initiates when $\tau_j \geq c_j + \sigma'_n \tan \varphi_j$ on the joint (where c_j is the joint cohesion), even a small tilt can turn into earlier and wider slip on one side and suppress it on the opposite side. This mechanism is clearly visible in the plot below:

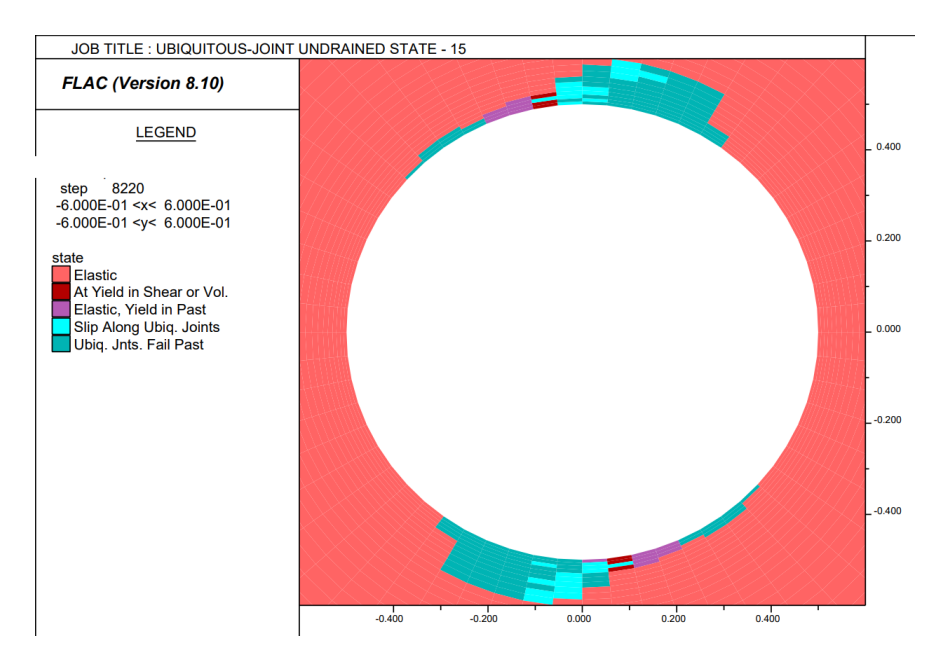


Figure 5.7: UBI undrained — state map for $\delta = 15^{\circ}$.

Tilt effect ($\delta = 15^{\circ}$). We noticed that, rotating the ubiquitous plane by 15° turn also the slip lobes and makes them asymmetric: one lobe widens and extends azimuthally, while the opposite shrinks. This indicates lower stability where the shear stress on the joint increases and the effective normal stress decreases. However, the mechanism remains joint—controlled; indeed, the joint areal extension is predominant with respect to matrix plasticity at the wall. Overall, the slipped area is slightly larger than that in the case of $\delta = 0^{\circ}$, i.e., translating into a reduction in wellbore stability. It's to be noted that, even in this scenario, the matrix undergoes shear in a limited portion.

5.1.5 CANISO, undrained $\delta = 0^{\circ}$

In the last model, introduced in this section, we will analyze in detail the effect of the weakness planes embedded in an elasto-plastic matrix.

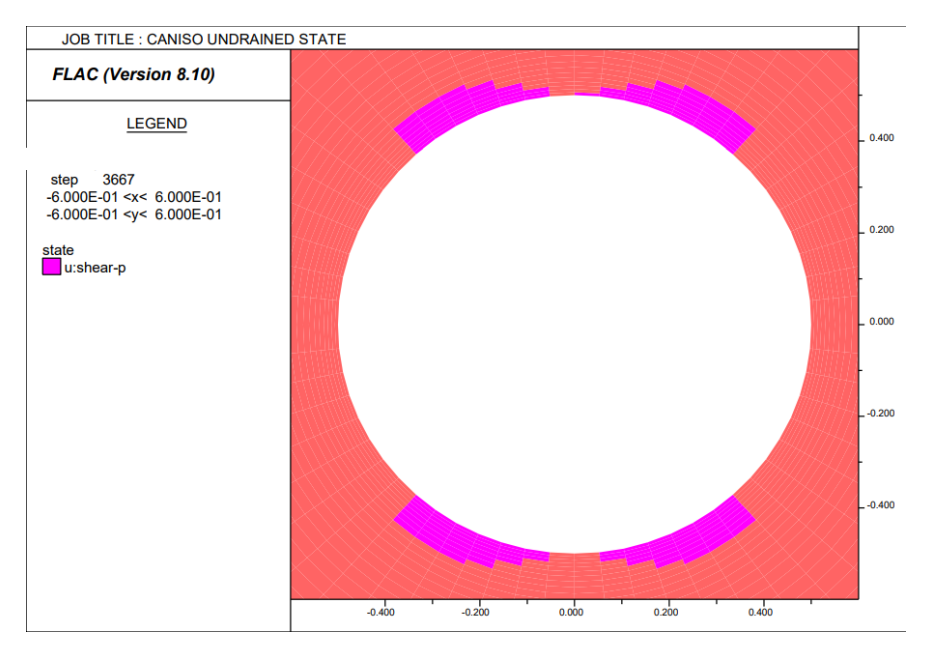


Figure 5.8: CANISO undrained — state map for $\delta = 0^{\circ}$.

Here, the tension/compression map is omitted because the wall remains fully in compression (no tensile visible with the standard grid ratio) adding no extra insights with respect to previous models.

Discussion. The Figure 5.8 shows two symmetric wall bands, marked with a Magenta color, which denote shear plasticity that is only governed by the weakness plane; indeed, the matrix results to be elastic elsewhere. With bedding parallel to the principal directions ($\delta = 0^{\circ}$), shear activation localizes in those two symmetric wall bands only, centered and mirrored near sector B. Plasticity is controlled only by the weakness plane (u:shear-p); the matrix remains essentially elastic at the end of the equilibrium. Compared with the UBI model, the onset azimuth is the same, but the bands look smoother and slightly more coherent, which clearly signals that the anisotropic stiffness is channeling the strain along the bedding planes.

Key takeaways. (i) When the CANISO model is subjected to the same load, weak-ness-plane shear at the wall predominates with respect to matrix yielding (compared to UBI). (ii) Transversely elastic isotropy tends to align the plastic zones with bedding, producing cleaner and more continuous bands compared to UBI.

5.1.6 CANISO, undrained $\delta = 15^{\circ}$

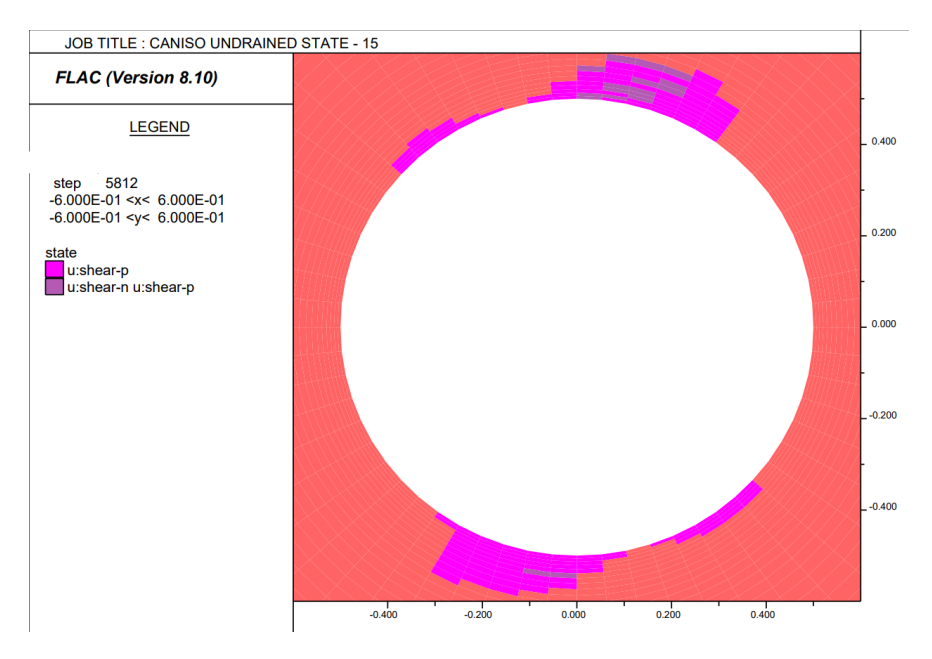


Figure 5.9: CANISO undrained — state map for $\delta = 15^{\circ}$.

Tilt effect ($\delta = 15^{\circ}$). When a 15° bedding tilt is set, the two shear bands lose symmetry and rotate azimuthally according to the tilt angle, confirming what has been said about the UBI model. The upper band becomes wider and more continuous, while the opposite one shrinks. In the most solicited side, zones of u:shear-n u:shear-p (violet) appear, indicating simultaneous mobilization of shear and normal plasticity on the weakness plane. This makes sense when you look at how stress works on a slanted surface: the shearing force τ_j grows while the effective normal stress σ'_n drops on one side. This means the rock will start to deform earlier with an extended yielding; the cross-anisotropic stiffness then channels deformation along bedding (as described in the CANISO with $\delta = 0^{\circ}$).

.

Key takeaways. (i) Overall, CANISO localizes plasticity almost entirely on the weak-ness plane, keeping the matrix in the elastic field. (ii) The introduction of a small tilt here $(\delta = 15^{\circ})$ makes yielding asymmetric and slightly more extensive, with local zones where both shear and normal components are mobilized on the joint. (iii) At the end, no tensile failure is detected; differences with UBI emerge in the coherence and directionality of the yielded bands due to elastic anisotropy.

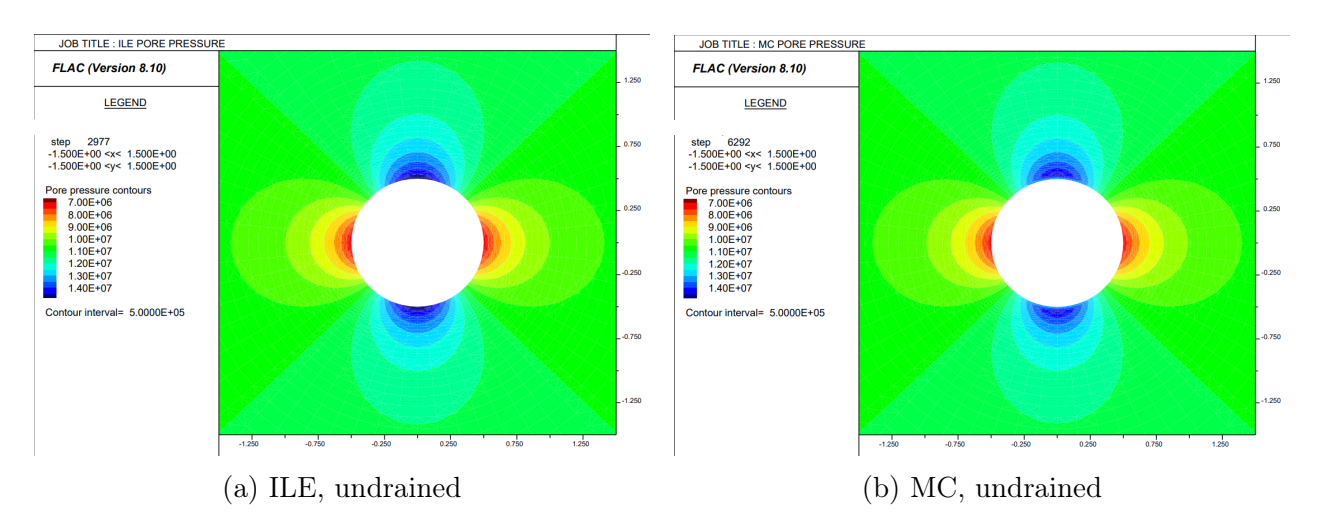
5.1.7 Cross-model recap and comparison

Here, we are going to collect and discuss the main outcomes of the undrained synthetic cases and highlight where models differ from each other.

Model comparison at the borehole wall. Our baseline in this comparison was the ILE run, which provided the elastic reference (no yielding) for the following models. The first plasticity effect is shown by Mohr–Coulomb, where narrow lobes at the wall in sector B were first identified. However, the MC predicted yielding in the rock matrix, which is not properly representative of the typical failure mechanism in shale formations. The introduction of the weakness planes under the Ubiquitous-Joint framework showed a slip along weak planes and pointed out that the main cause of failure is due to lower stiffness along them. The CANISO results, instead, show smoother yielded bands which seem more coherent, a direct consequence of elastic anisotropy channeling deformation along bedding, in agreement with UBI. Under the present overbalance $p_w > p_f$ all tension/compression maps remain compressive at the wall.

5.1.8 Undrained Analysis

Undrained pore pressure: common pattern. Across all models the pore-pressure maps display the same two-lobe response to the far-field stress contrast. Along sector B in which the hoop stress increases the most the rock skeleton compacts and the fluid pore pressure rises above p_f (blue lobes). This happens since the rock skeleton volume shrinks under deformation and the fluid (that cannot escape immediately) builds up the pressure to counterbalance this volume reduction. Vice versa, along sector A the skeleton unloads and pore pressure drops below p_f (red lobes). Because dilatancy is set to zero in both matrix and joints, plastic yielding does not add volumetric sources/sinks, so differences between ILE, MC, UBI and CANISO remain modest; elastic anisotropy in CANISO mainly sharpens.



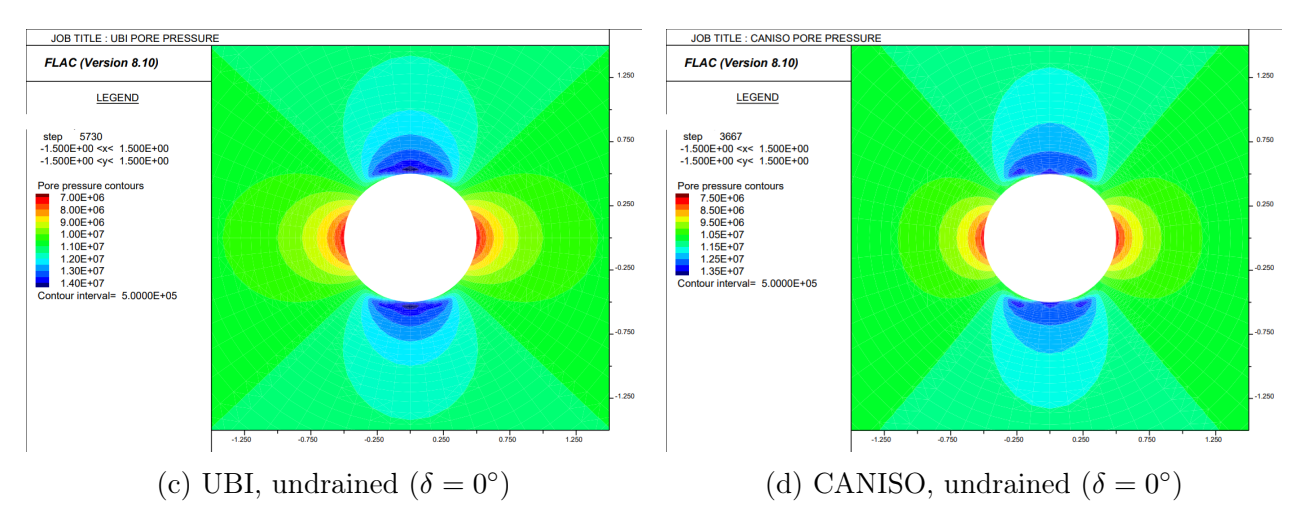


Figure 5.11: Undrained pore-pressure fields ($p_f = 11 \text{ MPa}$, $p_w = 14 \text{ MPa}$).

Comparison of pore–pressure plots. The same dipole pattern is shown for all four models in Fig. 5.11 with overpressure in sector B (blue) and underpressure in sector A (red/orange). The differences are mainly geometric. While the (a) ILE and (b) MC pore pressure plot practically overlap (smooth and symmetric lobes), because they share the same undrained poroelastic response; the shear yielding that appears in MC does not change volume and therefore does not reshape the p field.(c) UBI shows a sharper blue core in B and slightly tighter contours near the wall: weakness planes make the skeleton more compliant along bedding, concentrating deformation and thus the poroelastic Δp in that direction $\delta = 0$. (d) CANISO accentuates this focusing: transversely isotropic stiffness guides the strain, so the blue lobes in B appear slightly elongated/narrowed along the compliant direction, while the red lobes in A look more lens–shaped. In all cases p smoothly tends back to p_f away from the hole. The "detachment" observed in UBI/CANISO near the wellbore zone, is not a discontinuity nor induced flow along bedding planes, but it is due to a steeper gradient which is highlighted by the contouring.

Effect of bedding tilt. When a tilt angle is set $\delta = 15^{\circ}$ the lobes rotate proportionally; by doing so, a slight asymmetry is introduced as reported in in Fig. 5.12.

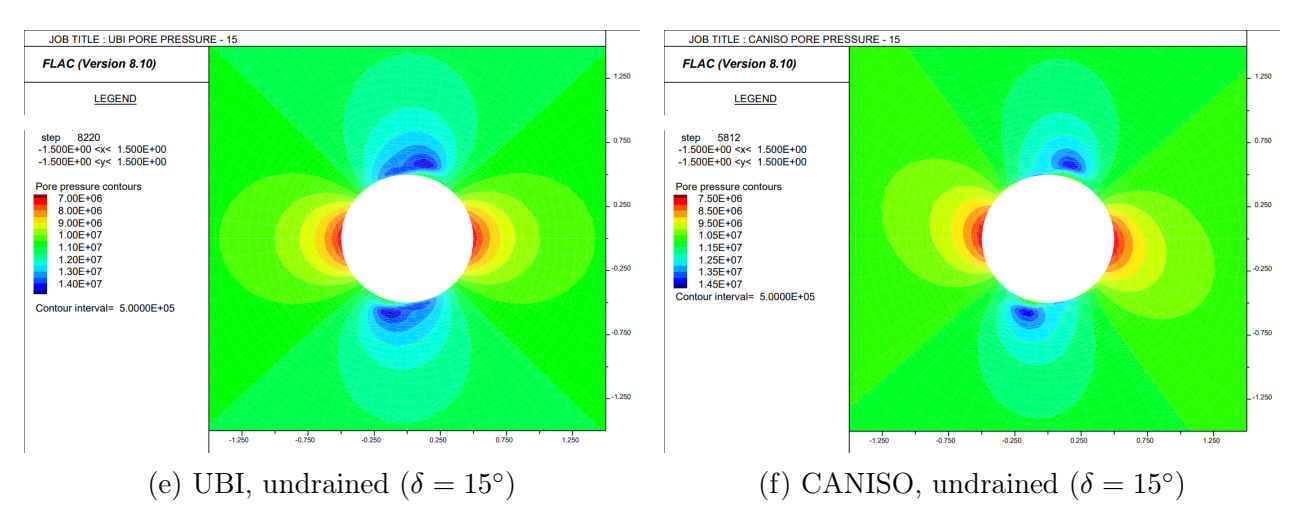


Figure 5.12: Undrained pore pressure with tilted bedding. Lobes rotate and become slightly asymmetric ($\delta = 15^{\circ}$)

Tilted bedding: UBI vs CANISO. In UBI (e), the positive (blue) and negative (red/orange) lobes are essentially the same as for $\delta = 0^{\circ}$ but rotated, with comparable amplitudes,

reflecting the joint orientation. In CANISO (f), the pattern both rotates and reshapes: elastic anisotropy makes the B-side overpressure lobe slightly more focused and the A-side underpressure lobe slightly more diffuse along the compliant direction. Overall magnitudes remain close to the $\delta=0^{\circ}$ cases; the dominant change is the azimuthal orientation and the lobe geometry.

5.2 Orientation Effects: Far-field Stress Swap δ^*

In this section we compare the UBI and CAN-ISO models under undrained conditions after swapping $\sigma_{H \max} \Leftrightarrow \sigma_{h \min}$; we do so, since these two models accounts for weakness planes which make their response direction-dependent and the comparisons interesting. The expected stress dipole and the yielding mechanisms should rotate by 90°: the overpressure lobes are supposed to move from sector B to A and the wall plasticity shifts accordingly. Moreover, to broaden the analysis drained conditions will be introduced in the model for the sake of completeness. Indeed, even though during drilling operation, as anticipated, shale behaves like an undrained rock, a study of fluid discharging from the pores will give a future-oriented analysis of stresses redistribution around the borehole walls.

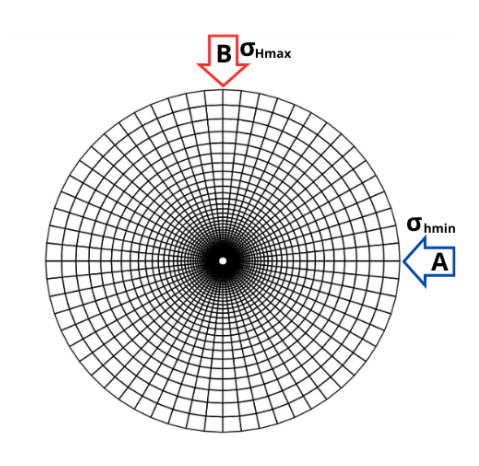


Figure 5.13: Far-field stresses swap

5.2.1 UBI, undrained: effect of far-field swap

In the Fig. 5.14 below are reported in (a) UBI under undrained condition, with $\sigma_{H,max}$ acting along the x-axis and $\sigma_{h,min}$ acting along the y-axis (already shown in the previous section but recalled for comparison purposes) and in (b) the introduction of swapped far-field stresses as illustrated in Fig. 5.13. Both (a) and (b) have the same bedding orientation $\delta = 0$.

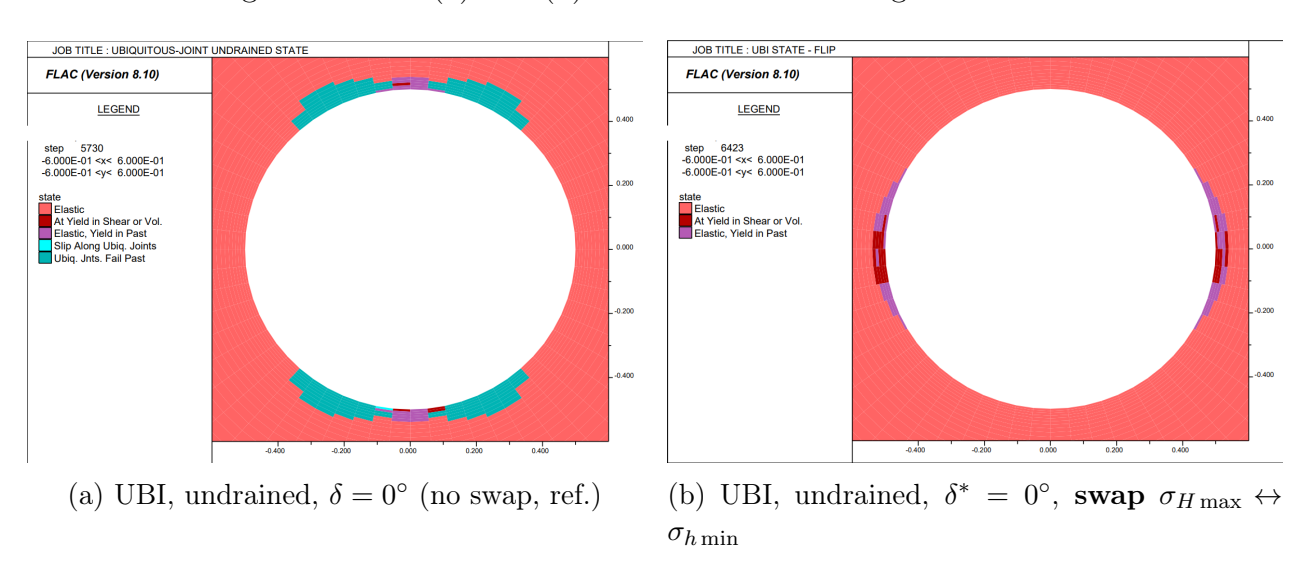


Figure 5.14: UBI — state map: undrained, effect of far-field swap at $\delta = 0^{\circ}$.

Discussion (UBI, $\delta = 0^{\circ}$). In the reference case (a) narrow joint–controlled slip zones developed around sector B, along with limited shear in the matrix, as already discussed in

Section 5.1.3. After swapping the far–field (b), the azimuth rotates: yielding appears where the new hoop maximum lies, but as we can appreciate, the dominance of weakness plane behavior we had is gone, leaving space for matrix-controlled plasticity which is denoted in the legend under the name of At Yield in Shear or Vol. / Yield in Past.

Physically, the peak hoop compression now acts nearly normal to bedding, which increases the effective normal stress on the weakness planes and suppresses slip along them. Thus, the main compressive stress conveys to the matrix, which shows the *At Yield in Shear or Vol.* and *Elastic, Yield in Past* as reported in the legend. This emphasizes the importance of considering such scenarios in anisotropic shales.

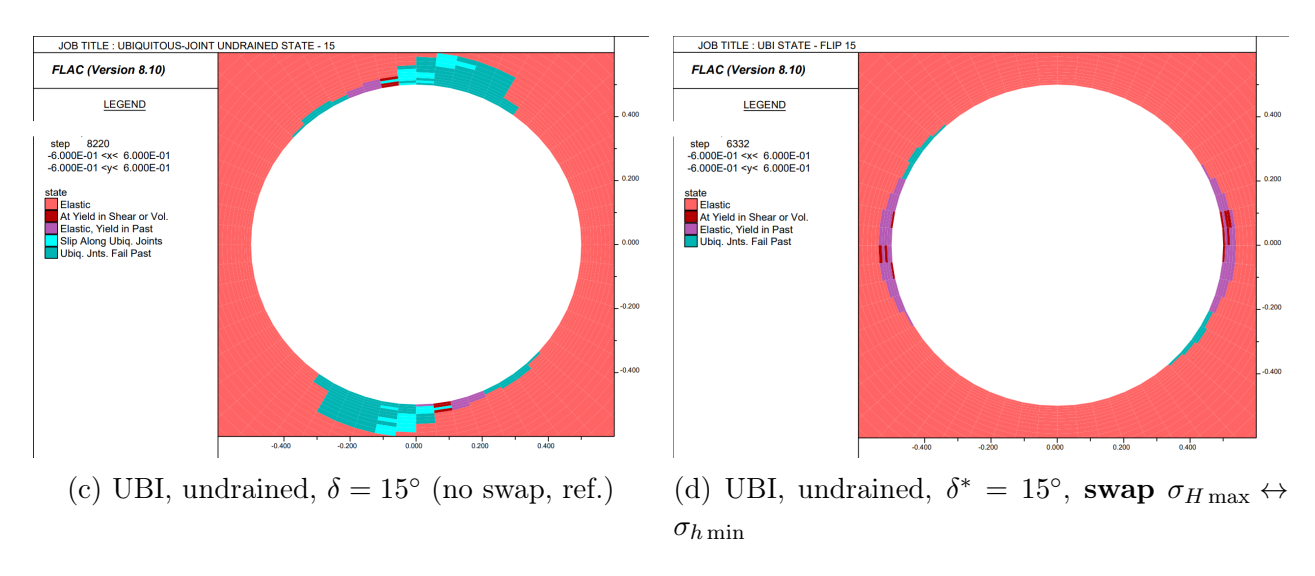


Figure 5.15: UBI — state map: undrained, effect of far-field swap at $\delta = 15^{\circ}$.

Discussion (UBI, $\delta = 15^{\circ}$). With a small tilt (c), the joint bands are asymmetric and more extended on the "favoured" side, as seen in Sec. 5.1.3. After the swap (d) the pattern rotates by $\simeq 90^{\circ}$, as in the previous scenario (without tilt) and the joint activity shrinks only to small patches of joint slippage (occurring in favorable zones to laminations' plane), while matrix past—yield stripes become prevalent. For these inputs, the joints are less solicited, hence the smaller slipped arc and the overall higher stability for both (b) and (d).

5.2.2 CANISO, undrained: effect of far-field swap

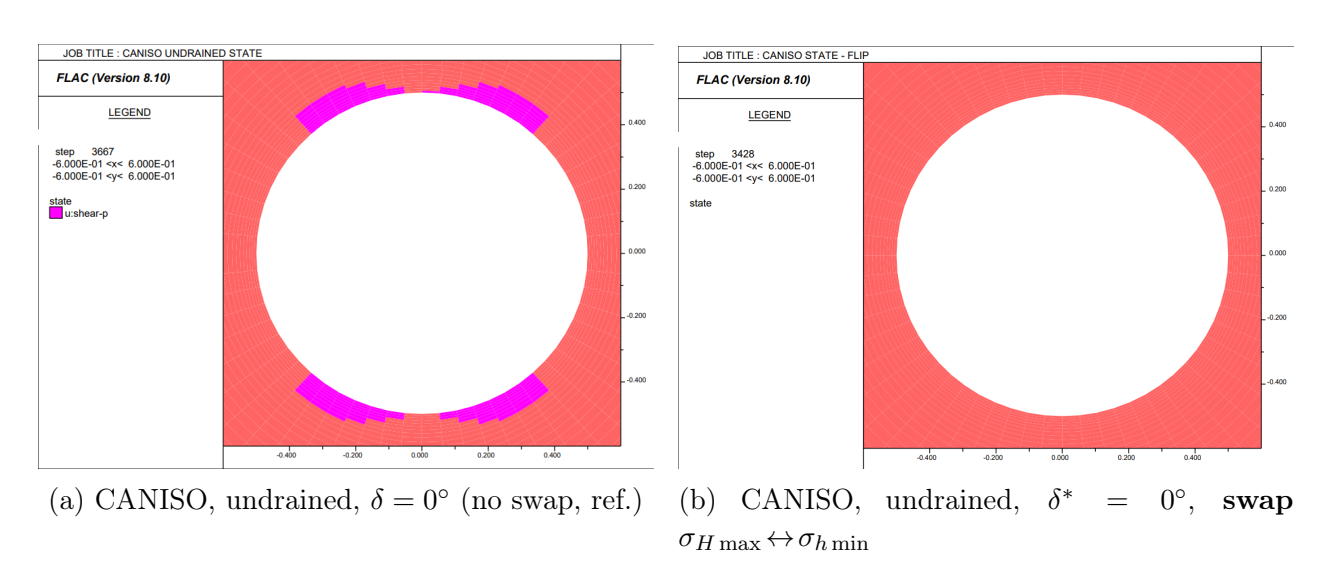


Figure 5.16: CANISO — state map: undrained, effect of far-field swap at $\delta = 0^{\circ}$.

Discussion CANISO, ($\delta = 0^{\circ}$). Here again, we have the reference case (a) in which two symmetric clean bands of *u:shear-p* form appears near B, fully controlled by the weakness plane. After the swap (b) the rotated loading is not able to mobilize the plane at the wall for these parameters: the map is essentially elastic. The transversely isotropic stiffness still channels deformation along bedding, but the resolved shear/normal combination on the plane is now insufficient for plastic activation — a clear *stabilizing* effect of the swap for $\delta = 0^{\circ}$.

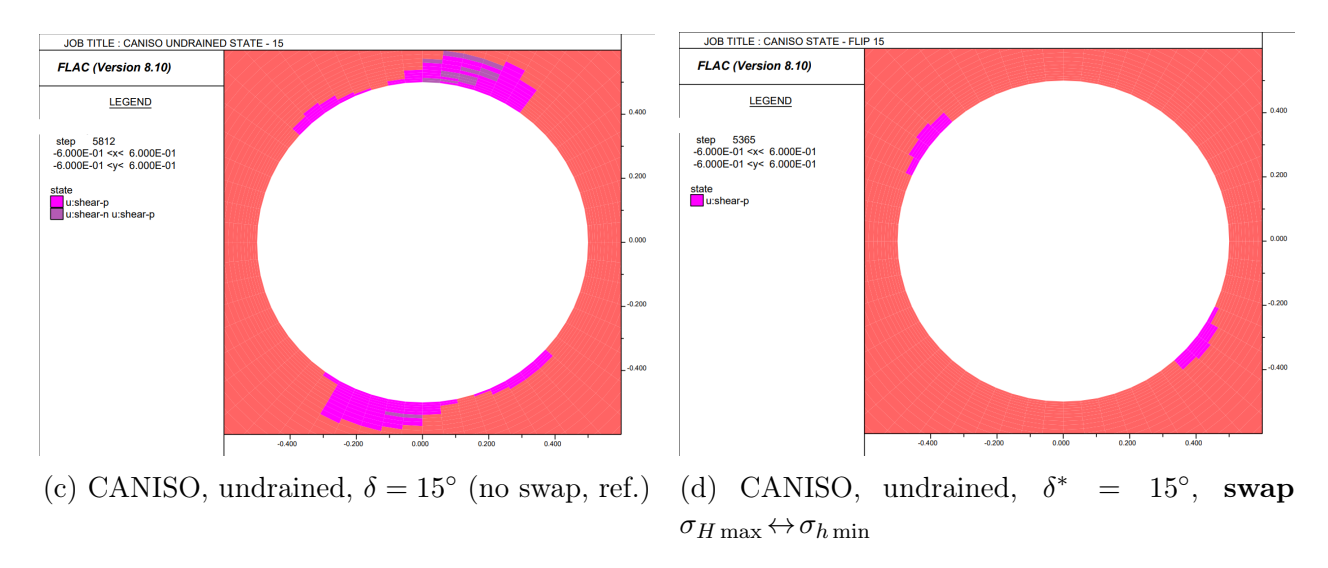


Figure 5.17: CANISO — state map: undrained, effect of far-field swap at $\delta = 15^{\circ}$.

Discussion CANISO, ($\delta = 15^{\circ}$). When tilted of 15° (c) the weakness–plane stripes result to be asymmetric, but still well defined. After swapping the tensions (d) the yielded sectors shorten to smaller arcs. Elastic anisotropy still focuses strain along bedding, but the new stress redistribution decreases the available shear on the plane; as a result, plasticity remains plane–controlled yet is less extensive with respect to the no–swap case.

Overall remarks (UBI vs CANISO under swap). As expected, both models register the 90° rotation due to the far–field swap. Here, the key difference lies in how much plasticity remains after the swap. Particularly, UBI keeps (in the case of δ^*) narrow matrix-dominated yielding; on the other hand, CANISO (under the same loading conditions) can become fully elastic at the matrix and have joint-controlled plasticity. In $\delta=15^\circ$ conditions, both show rotated, slightly asymmetric patterns, but the slipped/ yielded arcs result smaller than in the corresponding standard orientation cases.

5.3 UBI and CANISO — Undrained vs Drained

Until now we have analysed the short-term response of shale during drilling, i.e., undrained conditions. For completeness, we also compare the drained results, offering a broader view of longer exposure times of shale formations. We started from the UBI model and split the study into two parts: (i) the "normal" far-field stress orientation (undrained vs drained), and (ii) the swapped case, again comparing undrained and drained conditions. We then moved on to the CANISO model, adopting the same comparison scheme; however, since in the swapped case wall plasticity did not appear, we reduce the mud pressure to $p_w = 13$ to obtain a more informative comparison.

What we expect when moving from undrained to drained In undrained conditions, the pore fluid does not have time to diffuse during the short drilling window, so pore pressure

departs from the initial p_f value (overpressure and underpressure zones) and the effective stresses near the wellbore are reduced, especially in sector B, where overpressure builds up and slip/shear are easier to trigger. Conversely, in drained conditions pore pressure relaxes back toward p_f , effective stresses increase, and we expect smaller (or even vanishing) yielded/slip bands at the wall for the same loading.

5.3.1 UBI - Standard Orientation

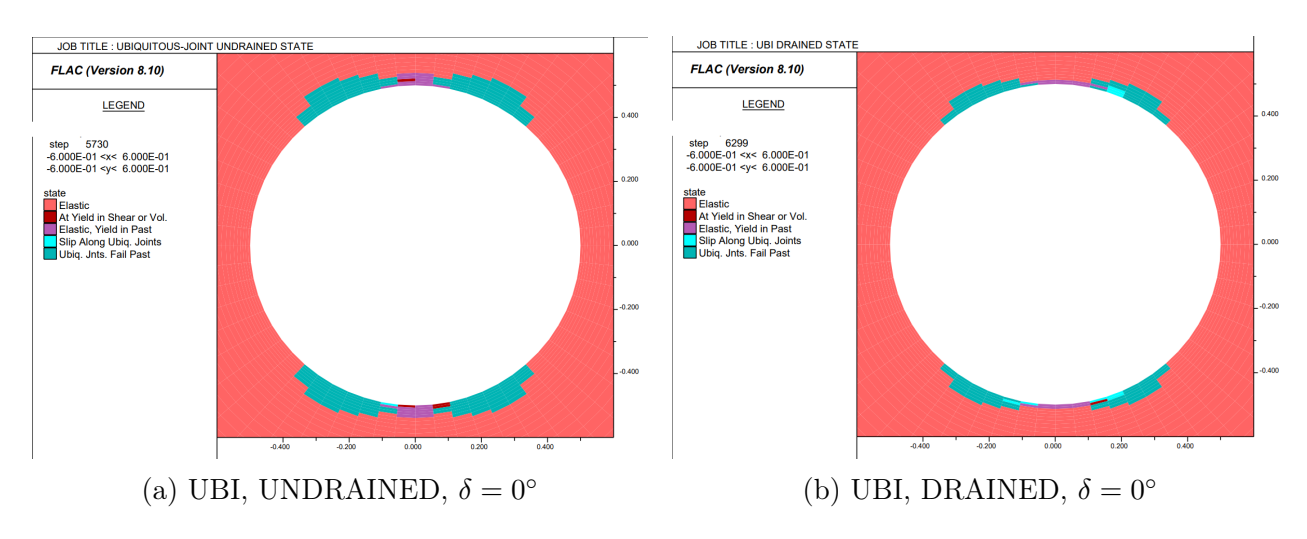


Figure 5.18: UBI — state map: undrained vs drained at $\delta = 0^{\circ}$.

Discussion UBI: undrained ref. vs drained (standard orientation) In the first set of figures (a) and (b) a comparison between (the already discussed in Section 5.1.3) undrained case and (the new) drained one is reported; both runs are under the "standard orientation" of the far-field stresses. Focusing on the drained condition, we can appreciate how the Sector B is still the most solicited, but a clear reduction of both joint-controlled and matrix yielding is observed in the near wellbore zone. Since the pore pressure (in drained conditions) is not constrained into the pore spaces, it flows out increasing the effective confinement and also the frictional strength. That's why the rock results to be more stable and the slip stripes shrink.

5.3.2 UBI - Swapped Orientation

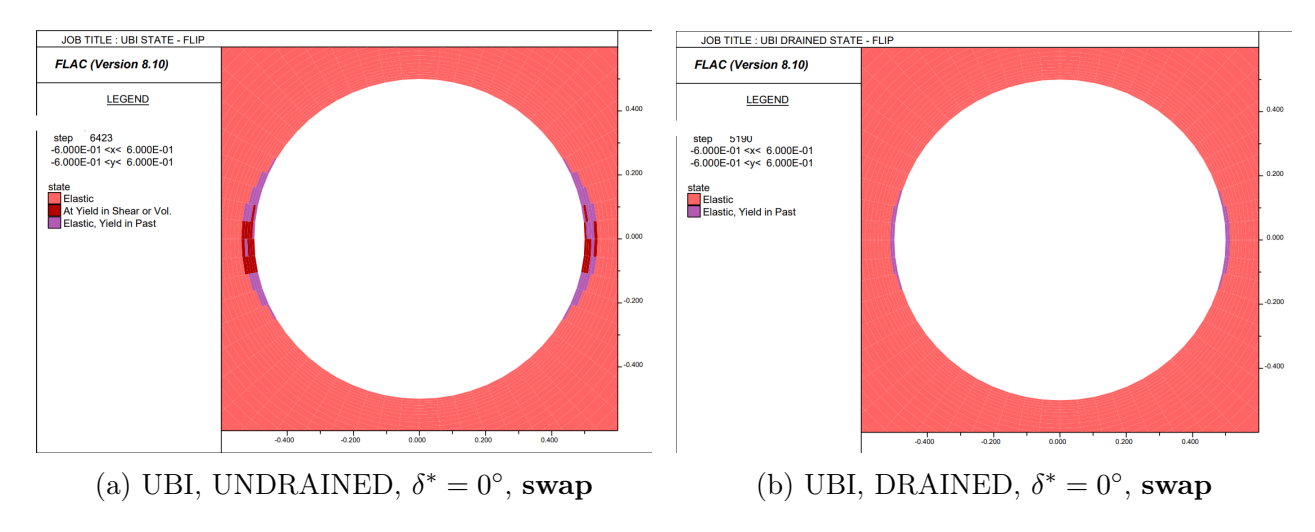


Figure 5.19: UBI — state map: swapped undrained vs drained at $\delta^* = 0^\circ$.

Discussion UBI: undrained ref. vs drained (swapped far-field stresses) The first state map relative to the undrained case (a) was already discussed in Section 5.2.1.In particular, after swapping $\sigma_{H,\text{max}} \leftrightarrow \sigma_{h,\text{min}}$ in UBI, we have observed the azimuthal rotation of plasticity along with matrix-dominated yielding. Moving from the undrained to drained conditions, as we can appreciate from case (b) shown in Figure 5.21, even though a matrix-controlled yield is still visible, it results to be slimmer and in the elastic domain. Hence, the matrix stripes shrink to vanish and Elastic, Yield in Past arcs fade. In summary, the swap suppresses plane slip and drainage removes the undrained overpressure and increases effective confinement, so under the same loading the wall response is almost fully elastic.

5.3.3 CANISO - Standard Orientation

Now we are moving to our last analysis in this thesis work, CANISO undrained vs drained, following the comparison roadmap used for UBI. In particular, here the matrix is purely elastic (transversely isotropic elastic as already said) and yielding is evaluated only on the weakness plane (i.e., slip is independent of any matrix plastic correction). Particularly, while in the standard orientation case we were able to perform a genuine comparison, moving to the swapped orientation, under the same conditions, yielding did not appear; therefore, we lowered the mud pressure (still in slight overbalance) until minimal yielding was observed.

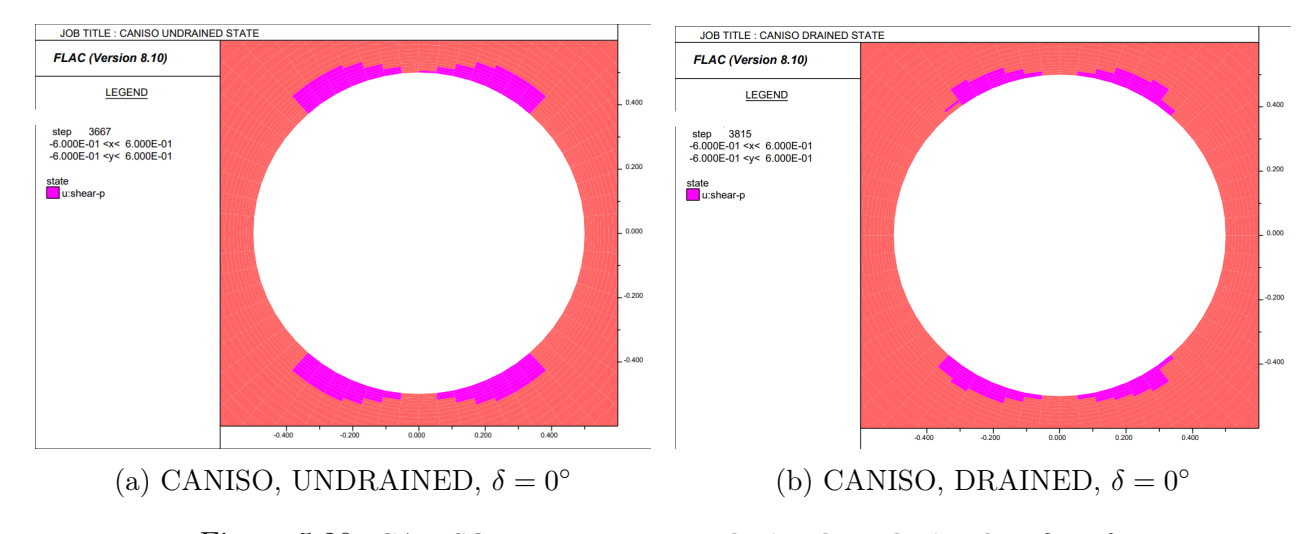


Figure 5.20: CANISO — state map: undrained vs drained at $\delta = 0^{\circ}$.

Discussion CANISO: undrained ref. vs drained (standard orientation) Following the same roadmap used in the UBI comparison, we discuss the main differences between the already seen undrained case and the (b) drained one; even here, the azimuthal location stays the same, but the stripes are visibly slimmer and shorter. Indeed, the shape of the yield zone is almost identical, but the damage is less severe. Thus, whenever we remove the undrained overpressure, the effective confinement increases and with it the general wellbore stability. Generally, the undrained condition resulted to be the most critical one in terms of borehole integrity, yet it is often ignored during drilling operations.

5.3.4 CANISO - Swapped Orientation

Under the swapped far-field stresses ($\sigma_{H,\text{max}} \leftrightarrow \sigma_{h,\text{min}}$) and the same mud pressure, the wall remained essentially elastic and no plastic zones were observed. To complete the comparison in a meaningful way, we therefore lowered p_w to 12.5 MPa, so that only a minimal amount of slip on the plane occurs at the wall. This allows us to ensure that the differences can be fairly compared.

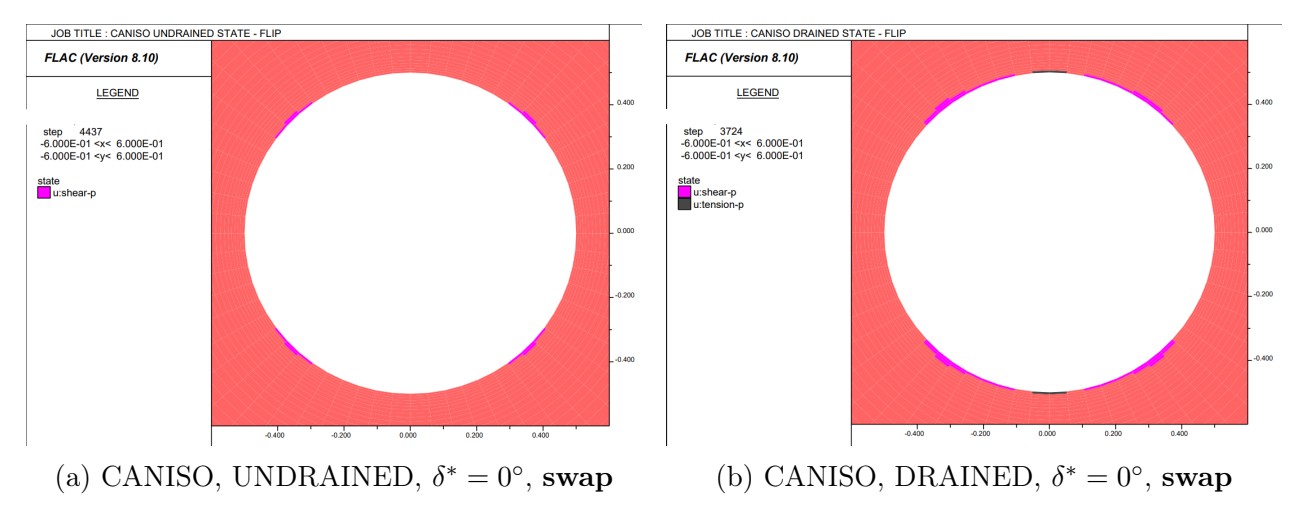


Figure 5.21: CANISO — state map: swapped undrained vs drained at $\delta^* = 0^\circ$, $p_w = 12.5$ MPa

Discussion — CANISO: swapped, undrained vs drained ($p_w = 12.5$ MPa) In the last comparison of this thesis work, the *undrained* CANISO model shows two short and coherent *u:shear-p* bands; in the *drained* case instead, the bands are slightly longer and in Sector B (which is now the axis holding the maximum far-field stress) a thin *u:tension-p* appears. This result suggests that when the pressure difference is close to zero, a slightly higher chance of joints opening could occur where the confinement is the minimum.

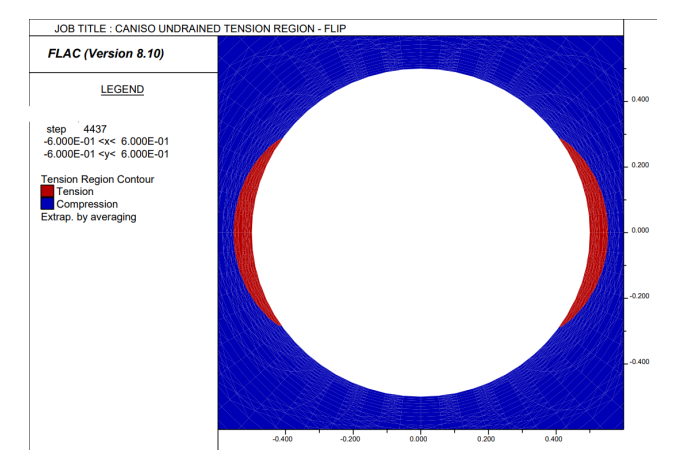


Figure 5.22: CANISO – Tension/compression map, swapped UNDRAINED case at $\delta^* = 0^\circ$, $p_w = 12.5$ MPa

Anyway, the undrained scenario evidences a tensile zone in the tension/compression map as shown in Figure 5.22; since this artifact can contaminate a direct comparison between drained and undrained conditions, we will not over-interpret the minor opening in sector B. Further validation such as mesh refinement or graded-ratio sweep would be useful to confirm the drained slivers are related to a numerical issue and not a physical one.

Conclusions

In this thesis work, we explored an interesting comparison between different constitutive models, to analyze the stress redistribution and the onset of failure near the wellbore using FLAC2D 8.1 software. We began with a general overview about shale mechanics and the reason why its remains important in a transitioning energy landscape. The concept of wellbore stability was then introduced to explain the primary goal of this geomechanical study: ensuring the integrity of the rock formation during drilling operations. In chapter 2, we established an analytical framework to better understand the subsequent numerical implementations; while in chapter 3, not only the Tournemire shale data were illustrated but also the constitutive laws were implemented in FLAC2D. Chapter 4 verified the numerical framework against the dry Kirsch solution. Lastly, in chapter 5: isotropic linear elastic (ILE), Mohr–Coulomb (MC), Ubiquitous Joint (UBI) and a cross-anisotropic elastoplastic (CAN-ISO) models were used to interpret the failure predictions among the presented synthetic cases.

Before any comparisons, a model validation was conducted to ensure the reliability of the results; in particular, a check between the analytical Kirsch's solution and the implemented ILE model under dry conditions was conducted. We then kept the same validated framework and increased model complexity to explore and isolate the role of plasticity in terms of both matrix and weakness planes. In the first set of synthetic cases (under undrained conditions), a slight overbalance was introduced, even though the mud pressure was reasonably lower than the MWW lower bound ($p_w = 14 \text{ MPa} > p_f = 11 \text{ MPa}$ so that all models shared the same poroelastic reference.

Synthetic case I: Undrained Conditions $\delta=0^\circ$: The models progressively increase in complexity. The ILE case was purely a diagnostic baseline, given that no matrix deformation occurs. The MC model was the first one to introduce plasticity in the matrix, shear was at first activated at the borehole wall in Sector B, with At Yield in Shear/Vol. zones and small Elastic, Yield in Past arcs. The latter indicate that the model, during its iterative process, hit the yield surface but the subsequent unloading phase occurred within elastic domain. Ubiquitous-joint is the first to introduce oriented weakness planes, here the failure prediction shifted primarily to slip along bedding than matrix, which is more consistent with shale physics where joints have lower shear resistance. The last model: CANISO, confirmed the UBI picture, but the transversal isotropic elastic behavior of the matrix channels the deformations mainly along bedding. Overall, all the models were in agreement and generally consistent throughout the complexity growth: ILE (elastic baseline) \rightarrow MC (matrix plasticity) \rightarrow UBI (joint-controlled plasticity) \rightarrow CANISO (elastic transversal anisotropy + joint-controlled).

In the end of this synthetic case comparison, an overview of pore-pressure behavior was conducted. Particularly, all the models showed the same dipole, in which $\Delta p > 0$, thus overpressure, in Sector B where the hoop compression is at its maximum, and $\Delta p < 0$

(underpressure) in Sector A. In our models, the dilatancy parameter was set to zero, and plasticity did not create any volumetric changes, so that the observed differences were geometric rather than in amplitude. When a small bedding tilt was introduced (UBI and CANISO) both state and Δp lobes tilted accordingly and slight asymmetry was observed.

Synthetic case II: Orientation Effects: In the second part of the discussion, we investigated the directional sensitivity by swapping $\sigma_{H,max} \Leftrightarrow \sigma_{h,min}$. Since this comparison is relevant only when a model accounts for weakness planes, only UBI and CANISO were included in the analysis. In UBI with $\delta^* = 0^\circ$ the yielding azimuth rotated by 90° as expected, but the joint-controlled behavior we observed before disappeared. Now the matrix is the primary initiator of shear, even if only on a smaller scale. Here, the new peak hoop (compression) acts normal to bedding, reducing the available shear there; the same logic holds in the $\delta^* = 15^\circ$ scenario, but a slight joint-slip shear is present, favored by the tilt. CANISO shows a different reaction after the "swap"; indeed, the state becomes entirely elastic. This happens because the stress is discharged onto the matrix, which is elastic by definition. In the last Synthetic case, we will see that we lowered the mud pressure down to $p_w = 12.5$ MPa to better evaluate wellbore stability.

Synthetic case III: Undrained vs Drained (UBI&CANISO: The last synthetic case focused on comparing UBI and CANISO under both undrained and drained conditions. Since drilling operations occur over a geologically short period, the rocks, especially those with low permeability such as shales, respond in an undrained manner. However, we included the drained conditions to complete the wellbore stability analysis by addressing the longerterm redistribution of stresses. For the UBI model, its behavior aligns with expectations: a reduction in plastic yielding is observed. This is because drainage allows the fluid to escape from the pore spaces and the effective confinement increases along with frictional strength. As a result, the rock and the wellbore integrity are more stable when drilled under these drained conditions. In contrast, CANISO model showed a different reaction after stress swap: the state map is now pure elastic. In order to observe any plasticity, we had to reduce the mud pressure to 12.5 MPa. In the final comparison, the undrained CANISO model generated two short u:shear-p bands; while, in the drained case, the bands were slightly longer and a thin u:tension-p band appeared in Sector B now holding the maximum far-field stress). Because these small-tensile zones showed up only under this specific settings, a further investigation may be required. Nevertheless, they indicate the possibility of a more brittle failure in the drained state along that specific azimuth.

Appendices

Nomenclature

Maximum principal stress [MPa]
Minimum principal stress [MPa]
Radial stress [MPa]
Hoop (tangential) stress [MPa]
Axial stress [MPa]
Maximum in-situ horizontal stress [MPa]
Minimum in-situ horizontal stress [MPa]
Effective stress (Terzaghi/Biot) [MPa]
Effective normal stress on weakness plane [MPa]
Shear stress on weakness plane [MPa]
Pore pressure far field [MPa]
Mud pressure at the borehole wall [MPa]
Excess pore pressure (undrained) [MPa]
Uniaxial compressive strength [MPa]
Uniaxial tensile strength [MPa]
Cohesion (matrix) [MPa]
Cohesion on weakness plane [MPa]
Friction angle (matrix) [°]
Friction angle on weakness plane [°]
Biot coefficient [–]
Young's modulus (parallel to bedding) [GPa]
Young's modulus (normal to bedding) [GPa]

- G_{hv} Shear modulus (h–v plane) [GPa] ν_{hh} Poisson's ratio (in bedding) [–]
- ν_{vh} Poisson's ratio (vertical–to–horizontal) [–]
- R_w Borehole radius [m]
- r Radial coordinate [m]
- θ Azimuth from $\sigma_{H,\max}$ [°]
- δ Bedding tilt w.r.t. principal stresses [°]
- δ^* Far-field principal-stress flip indicator [–]
- β_w Angle between weakness plane and borehole axis [°]

Bibliography

- [1] Dodson, J., Dodson, T., & Schmidt, V. (2004). Gulf of Mexico "trouble time" creates major drilling expenses: Use of cost-effective technologies needed. Offshore, 64(1). [CrossRef]
- [2] Li, S., Zhou, P., & Lan, B. (2024). Study of wellbore instability in shale formation considering the effect of hydration on strength weakening. Frontiers in Earth Science, 12, 1403902. [CrossRef]
- [3] Acemoglu, D., Briggs, R., Linn, J., Ozimek, A., Restrepo, P., & Syverson, C. (2023). Climate change, directed innovation, and energy transition: The long-run consequences of the shale gas revolution (NBER Working Paper No. 31657). National Bureau of Economic Research. [CrossRef]
- [4] U.S. Energy Information Administration. (2011). Shale gas provides largest share of U.S. natural gas production (Today in Energy). [CrossRef]
- [5] Sadkhan, R. A., & Al-Mudhafar, W. J. (2024). Key aspects of underground hydrogen storage in depleted hydrocarbon reservoirs and saline aquifers: A review and understanding. Energy Geoscience, 100339. [CrossRef]
- [6] Peter, A., Zhao, Z., Wang, S., Sun, J., & Wang, Z. (2022). A review of the studies on CO_2 -brine-rock interaction in geological storage process. Geosciences, 12(4), 168. [CrossRef]
- [7] Benetatos, C., Perotti, C. R., Giovine, L., Santarelli, F., Di Toro, G., Ravagnan, S., & Collettini, C. (2023). Deformation behavior of a regional shale formation from integrated laboratory and well data analysis: Insights for underground fluid storage in northern Italy. Geoenergy Science and Engineering, 229, 212109. [CrossRef]
- [8] Hou, L., Teng, M., Zhao, Y., Zhou, X., & Chen, Y. (2024). Feasibility and prospects of symbiotic storage of CO_2 and H_2 in shale reservoirs. Renewable and Sustainable Energy Reviews, 189, 113878. [CrossRef]
- [9] Zhang, J. (2013). Borehole stability analysis accounting for anisotropies in drilling to weak bedding planes. International Journal of Rock Mechanics and Mining Sciences, 60, 160-170. [CrossRef]
- [10] Asquith, G., & Krygowski, D. (2004). Basic well log analysis (2nd ed.). AAPG (Methods in Exploration Series 16). [CrossRef]
- [11] Tingay, M. R. P., Reinecker, J., & Müller, B. (2016). Guidelines for borehole breakout and drilling-induced fracture analysis from image logs. In O. Heidbach et al. (Eds.), WSM Technical Report 16-01: WSM quality ranking scheme, database description and analysis guidelines for stress indicator. GFZ German Research Centre for Geosciences. [CrossRef]

- [12] osh, M., Esteban, L., Delle Piane, C., Sarout, J., Dewhurst, D. N., & Clennell, M. B. (2012). Laboratory characterisation of shale properties. Journal of Petroleum Science and Engineering, 88–89, 107–124. [CrossRef]
- [13] Risnes, R. (2001). Deformation and yield in high porosity outcrop chalk. Physics and Chemistry of the Earth, Part A: Solid Earth and Geodesy, 26(1–2), 53–57. [CrossRef]
- [14] Abousleiman, Y. N., Tran, M. H., Hoang, S. K., Bobko, C. P., Ortega, J. A., & Ulm, F.-J. (2007, November). Geomechanics field and laboratory characterization of Woodford Shale: The next gas play (SPE Paper 110120). SPE Annual Technical Conference and Exhibition. [CrossRef]
- [15] Wöhrl, B., Wessling, S., Bartetzko, A., Pei, J., & Renner, J. (2010). Comparison of methods to derive rock mechanical properties from formation evaluation logs. In Proceedings of the 44th U.S. Rock Mechanics Symposium (ARMA 10-167). American Rock Mechanics Association. [CrossRef]
- [16] Asaka, M., & Holt, R. M. (2021). Anisotropic wellbore stability analysis: Impact on failure prediction. Rock Mechanics and Rock Engineering, 54, 583–605. [CrossRef]
- [17] Aoki, T., Tan, C. P., & Bamford, W. E. (1993). Effects of deformation and strength anisotropy on borehole failures in saturated shales. International Journal of Rock Mechanics and Mining Sciences & Geomechanics Abstracts, 30(7), 1031–1034. [CrossRef]
- [18] Domenico, P. A., & Schwartz, F. W. (1997). Physical and chemical hydrogeology (2nd ed.). John Wiley & Sons. *Physical and Chemical Hydrogeology*. 2nd Edition, John Wiley & Sons, New York.
- [19] Detournay, E., & Atkinson, C. (2000). Stress-dependent permeability of the rock mass around a deep wellbore. International Journal of Rock Mechanics and Mining Sciences, 37(1–2), 123–137. [CrossRef]
- [20] Tran, N. H., Santarelli, F. J., & Bérard, T. (2022). Combined effect of anisotropy and uncertainty on the safe mud pressure window in wellbore stability analysis. International Journal of Rock Mechanics and Mining Sciences, 150, 104716. [CrossRef]
- [21] Li, C., Zhan, L., & Lu, H. (2022). Mechanisms for overpressure development in marine sediments. Journal of Marine Science and Engineering, 10(4), 490. [CrossRef]
- [22] Fjaer, E., Holt, R. M., Horsrud, P., Raaen, A. M., & Risnes, R. (2008). Petroleum related rock mechanics (2nd ed.). Elsevier. ISBN 978-0-444-50260-5. [CrossRef]
- [23] Abdi, H., Labrie, D., Nguyen, T. S., Barnichon, J.-D., Su, G., Evgin, E., Simon, R., & Fall, M. (2015). Laboratory investigation on the mechanical behaviour of Tournemire argillite. Canadian Geotechnical Journal, 52(3), 268–282. [CrossRef]